Journal of the Mechanics and Physics of Solids 58 (2010) 1776–1803

Contents lists available at ScienceDirect

Journal of the Mechanics and Physics of Solids

journal homepage: www.elsevier.com/locate/jmps

Microscopic and macroscopic instabilities in finitely strained fiber-reinforced elastomers

J.C. Michel [a], O. Lopez-Pamies [b], P. Ponte Castañeda [c], N. Triantafyllidis [d,e,*]

[a] Laboratory of Mechanics and Acoustics, 31 Chemin Joseph Aiguier, Marseille 13402, France
[b] Department of Mechanical Engineering, State University of New York, Stony Brook, NY 11794-2300, USA
[c] Department of Mechanical Engineering and Applied Mechanics, The University of Pennsylvania, Philadelphia, PA 19104-6315, USA
[d] Laboratory of Solid Mechanics and Department of Mechanics, Ecole Polytechnique, Palaiseau 91128, France
[e] Department of Aerospace Engineering, The University of Michigan, Ann Arbor, MI 48109-2140, USA

ARTICLE INFO

Article history:
Received 19 May 2010
Received in revised form
19 August 2010
Accepted 21 August 2010

Keywords:
Fiber-reinforced material
Elastic material
Finite strain
Stability and bifurcation
Finite elements

ABSTRACT

The present work is a detailed study of the connections between microstructural instabilities and their macroscopic manifestations — as captured through the effective properties — in finitely strained fiber-reinforced elastomers, subjected to finite, plane-strain deformations normal to the fiber direction. The work, which is a complement to a previous and analogous investigation by the same authors on porous elastomers, (Michel et al., 2007), uses the linear comparison, second-order homogenization (S.O.H.) technique, initially developed for random media, to study the onset of failure in periodic fiber-reinforced elastomers and to compare the results to more accurate finite element method (F.E.M.) calculations. The influence of different fiber distributions (random and periodic), initial fiber volume fraction, matrix constitutive law and fiber cross-section on the microscopic buckling (for periodic microgeometries) and macroscopic loss of ellipticity (for all microgeometries) is investigated in detail. In addition, constraints to the principal solution due to fiber/matrix interface decohesion, matrix cavitation and fiber contact are also addressed. It is found that both microscopic and macroscopic instabilities can occur for periodic microstructures, due to a symmetry breaking in the periodic arrangement of the fibers. On the other hand, no instabilities are found for the case of random microstructures with circular section fibers, while only macroscopic instabilities are found for the case of elliptical section fibers, due to a symmetry breaking in their orientation.

1. Introduction and motivation

Failure in composite materials is a fundamental as well as an extremely diverse issue in solid mechanics. Questions about what constitutes failure, when does failure start and whether it is possible to predict the onset of failure by investigating the effective (homogenized) properties of the solid, are problems of fundamental interest for all composites. The infinite variety of matrix materials and microstructures, which result in a multitude of possible failure mechanisms, is the reason for the problem's extraordinary diversity. In the interest of (relative) simplicity, and motivated by considerable recent advances in calculating the effective properties of finitely strained nonlinear solids, attention is focused here on particle-reinforced elastomers. To further simplify this complex problem, only two-dimensional such elastomers are

* Corresponding author at: Laboratory of Solid Mechanics and Department of Mechanics, Ecole Polytechnique, Palaiseau 91128, France.
E-mail address: nick@lms.polytechnique.fr (N. Triantafyllidis).

0022-5096/$ - see front matter © 2010 Elsevier Ltd. All rights reserved.
doi:10.1016/j.jmps.2010.08.006

considered here, which can also be viewed as fiber-reinforced elastomers under in-plane loading perpendicular to their fiber axes. Even this particular class of composites is of considerable practical interest and enjoys a wide range of technological applications, e.g., car tires, many types of biological tissues and block copolymers with cylindrical microstructures, just to name a few. A brief review of the relevant literature in finitely strained inclusion-reinforced elastomers is presented here, with particular emphasis on the associated stability issues for the case of random as well as periodic microgeometries.

To relate the onset of failure in these composites to their effective properties, one must address the issues of homogenization and of microstructure stability. On the homogenization front, a considerable effort has been devoted to predict the effective properties of hyperelastic composites with random microstructures, starting with the work of Hill (1972). The homogenization of these solids presents serious technical challenges which were addressed in a series of papers by Ponte Castañeda and co-workers, starting with Ponte Castañeda (1989). From the increasingly accurate homogenization schemes which have been subsequently devised, of particular interest here are the second-order homogenization methods originally introduced by Ponte Castañeda (1996, 2002) in the context of small strain nonlinear elasticity. The first of these methods makes use of a tangent linearization evaluated at the phases averages of the deformation fields, while the second makes use of generalized secant linearization, additionally taking into account the covariance of the fluctuations of the deformation field. These techniques have been extended to finite-strain elasticity and applied to particle-reinforced elastomers by Ponte Castañeda and Tiberio (2000) and by Lopez-Pamies and Ponte Castañeda (2006a,b). The resulting models are sophisticated enough to account for the evolving microstructure and are thus capable of predicting a macroscopic material failure in the form of a loss of strong ellipticity (or rank-one convexity) of the corresponding homogenized behavior.

On the microstructural stability side, an intimate connection was discovered between the onset of microscopic buckling and the corresponding loss of ellipticity of the incremental moduli in the homogenized solid. This was first shown by Triantafyllidis and Maker (1985) for an incompressible, hyperelastic layered composite under plane-strain. Subsequent work by Geymonat et al. (1993) established a rigorous connection between bifurcation instability at the microscopic level and loss of rank-one convexity of the homogenized moduli in finitely strained periodic elastomers of infinite extent. More specifically, it was shown that if the wavelength of the bifurcation eigenmode is infinite (compared to the unit cell size), the corresponding instability of the periodic principal solution can be detected as a loss of ellipticity of the one-cell homogenized tangent moduli of the solid. Based on these general results, Triantafyllidis and Bardenhagen (1996) defined the onset-of-failure surfaces in stress and strain space for periodic solids of infinite extent, a concept which was subsequently applied among other solids to the case of honeycomb by Triantafyllidis and Schraad (1998), of fiber-reinforced composites under combined normal and shear strains by Nestorović and Triantafyllidis (2004), to three-dimensional Kelvin foams Gong et al. (2005) and more recently to two-dimensional periodic elastomers with circular inclusions of variable stiffness-to-matrix ratios by Triantafyllidis et al. (2006).

The present work is a complement to a recent, comprehensive investigation by the same authors on porous elastomers (Michel et al., 2007), and provides a detailed study of the connections between microstructural instabilities and their macroscopic manifestations — as captured through the effective properties — in finitely strained fiber-reinforced elastomers, subjected to finite, plane-strain deformations normal to the fiber direction. The work uses the above-mentioned second-order homogenization (S.O.H.) technique, to study the onset of failure in periodic fiber-reinforced elastomers and to compare the results to more accurate finite element method (F.E.M.) calculations. The influence of different fiber distributions (random and periodic), initial fiber volume fraction, matrix constitutive law and fiber cross-section on the microscopic buckling (for periodic microgeometries) and macroscopic loss of ellipticity (for all microgeometries) is investigated in detail. In addition, constraints to the principal solution due to fiber/matrix interface decohesion, matrix cavitation and fiber contact are also addressed, thus giving a complete picture of the different possible failure mechanisms present in this class of elastomeric composites.

The presentation of the work is organized as follows. Section 2 deals with the general, three-dimensional theoretical considerations for the effective properties of inclusion-reinforced elastomers, the relation between microscopic instabilities and macroscopic loss of ellipticity (for periodic microstructures) as well as the definition of the onset-of-failure surfaces. The description of the loading path and the presentation of the different (two-dimensional) calculation methods (the second-order homogenization method with associated linear comparison solid, as well as the finite element method) is given in Section 3. The specific matrix constitutive choices and the results of the calculations for some representative fiber-reinforced elastomers are presented and discussed in Section 4 followed by the conclusion in Section 5. Finally, the additional constraints on the effective response of these elastomers (fiber/matrix interface decohesion, matrix cavitation and fiber contact) are addressed in Appendix A while the expressions for the microstructural tensor $\mathbf{P}$, which is required for the homogenization calculations, are given for different microgeometries in Appendix B.

2. Theoretical considerations

As stated in the Introduction, the goal of this work is to study the instabilities of inclusion-reinforced, elastic solids subjected to finite-strain loading conditions. Of particular interest here is the microscopic (local) instability information that can be extracted by investigating the macroscopic (homogenized) properties of fiber-reinforced elastomers and the

influence of microgeometry and matrix material on the stability of these solids. The concepts introduced in this section are general and apply to two- or three-dimensional inclusion-reinforced elastomers with arbitrary shape inclusions (with fibers being a special case of an inclusion) and pointwise rank-one convex inclusion and matrix constitutive laws.

The first subsection deals with the macroscopic properties of inclusion-reinforced elastomers and the related concept of *macroscopic stability*, which is based on the fact that the equilibrium solution of a *representative volume element* (RVE) under Dirichlet boundary conditions is a local minimizer of the RVE's energy. This criterion leads to the strong ellipticity of the homogenized solid's incremental moduli or, equivalently, to the *strict* rank-one convexity of the homogenized stored-energy function.

The second subsection pertains to the stability of periodic inclusion-reinforced elastomers. For solids with periodic microstructures, a simple unit cell can be easily identified and accurate numerical homogenization calculations can be accomplished based on this unit cell. The question that naturally arises is whether for a given macroscopic load, the energy minimizing solution is periodic with period the chosen unit cell, or whether a different energy minimizer exists which is periodic on a larger cell. To this end, the concept of *microscopic stability* is introduced, which is based on the examination of all bounded perturbations in the infinite solid about the periodic equilibrium solution under consideration. The microscopic stability investigation makes use of the chosen unit cell in conjunction with a Bloch-wave technique.

Following the above stability definitions, the concept of a microscopic and a macroscopic *onset-of-failure surface* in macroscopic load space is introduced in the third subsection. For random microgeometries only the macroscopic onset-of-instability surface can be defined. For periodic microstructures, both onset-of-failure surfaces (i.e., the microscopic and the macroscopic surfaces) can be found and the former surface lies by definition inside the latter. The microscopic onset-of-failure surfaces can also be used to characterize the domain in macroscopic load space where the homogenized properties based on calculations using the chosen unit cell are valid and coincide with the homogenized properties calculated using an infinite number of cells.

2.1. Macroscopic properties and stability of inclusion-reinforced elastomers

Consider a reinforced elastomer made up of disconnected inclusions that are distributed, either with periodic or random microstructure, in an elastomeric matrix phase. A specimen of this inclusion-reinforced material is assumed to occupy a volume Ω_0 in the reference configuration, in such a way that the typical size of the inclusions is much smaller than the size of the specimen and the scale of variation of the applied loading. Thus, in the homogenization limit (i.e., in the limit as the size of the inclusions goes to zero), Ω_0 can be identified with a *representative volume element* (RVE) of the inclusion-reinforced elastomer.

Some useful notation is in order; the average of a field quantity $\mathbf{f}$, denoted by $\langle \mathbf{f} \rangle$ is defined by

$$\langle \mathbf{f} \rangle \equiv \frac{1}{\Omega_0} \int_{\Omega_0} \mathbf{f}(\mathbf{X})\, d\mathbf{X}. \tag{2.1}$$

Material points in the solid are identified by their initial position vector $\mathbf{X}$, while the current position vector of the same point is denoted by $\mathbf{x}$. The displacement of each material point $\mathbf{X}$ is denoted by $\mathbf{u}$, such that $\mathbf{u} \equiv \mathbf{x} - \mathbf{X}$. The deformation gradient $\mathbf{F}$ at $\mathbf{X}$, a quantity that measures the deformation in the neighborhood of $\mathbf{X}$, is defined as

$$\mathbf{F} \equiv \mathbf{x}\nabla = \mathbf{I} + \mathbf{u}\nabla, \quad (F_{ij} \equiv \partial x_i/\partial X_j = \delta_{ij} + \partial u_i/\partial X_j). \tag{2.2}$$

The constitutive behavior of the hyperelastic matrix phase, which occupies the subdomain $\Omega_0^{(1)}$, is characterized by a stored-energy function $W^{(1)}$ that is a *non-convex* function of the deformation gradient $\mathbf{F}$. The constitutive behavior of the inclusion phase, which occupies the subdomain $\Omega_0^{(2)}$, is described by the stored-energy function $W^{(2)}$ which is also a *non-convex* function of the deformation gradient $\mathbf{F}$. Since rigid fiber inclusions are of ultimate interest here, we henceforth assume $W^{(2)} = \eta W^{(1)}$, where $\eta > 0$ is a large positive constant (typically of the order of 10^3).[1] Thus, the local energy function of this two-phase system may be written as

$$W(\mathbf{X}; \mathbf{F}) = \sum_{r=1}^{2} \chi_0^{(r)}(\mathbf{X}) W^{(r)}(\mathbf{F}). \tag{2.3}$$

Here the functions $\chi_0^{(1)}$, equal to 1 if the position vector $\mathbf{X} \in \Omega_0^{(1)}$ and zero otherwise, and $\chi_0^{(2)}$, equal to 1 if the position vector $\mathbf{X} \in \Omega_0^{(2)}$ and zero otherwise, describe the distribution of the two phases in the reference configuration of the hyperelastic inclusion-reinforced solid. The two phases are related by $\chi_0^{(2)} = 1 - \chi_0^{(1)}$. Henceforth, for simplicity, the matrix-related symbols χ_0 and W are used instead of $\chi_0^{(1)}$ and $W^{(1)}$.

The characteristic function χ_0 may be periodic or random. In the first case, the dependence of χ_0 on the position vector $\mathbf{X}$ is completely determined once a unit cell D has been specified. In the second case, the dependence of χ_0 on $\mathbf{X}$ is not known precisely, and the microstructure is only partially defined in terms of the n-point statistics of the system. Here, use will be made of information up to only two-point statistics in order to be able to take advantage of linear homogenization

[1] The generality of this section is not impaired by this assumption, one can consider any $W^{(2)} \neq W^{(1)}$, as long as they are both strictly rank-one convex functions of $\mathbf{F}$.

estimates that are available from the literature. It is noted that the initial volume fraction of the matrix phase is given by $\langle \chi_0 \rangle$, hence the initial volume fraction of the inclusion phase can be defined by $f_0 \equiv 1-\langle \chi_0 \rangle$.

The stored-energy function of each phase will, of course, be assumed to be *objective* in the sense that $W(Q_{ik}\,F_{kj})=W(F_{ij})$ for all proper orthogonal $\mathbf{Q}$ and arbitrary deformation gradients $\mathbf{F}$. Making use of the polar decomposition $F_{ij}=R_{ik}U_{kj}$, where $\mathbf{U}$ is the right stretch tensor and $\mathbf{R}$ is the rotation tensor, it follows, in particular, that $W(\mathbf{F}) = W(\mathbf{U})$. The constitutive relation of the matrix material is

$$\mathbf{S} = \frac{\partial W}{\partial \mathbf{F}}(\mathbf{F}), \quad \left(S_{ij} = \frac{\partial W}{\partial F_{ij}}(\mathbf{F})\right), \tag{2.4}$$

where $\mathbf{S}$ denotes the *nominal* stress tensor (the transpose of the *first Piola–Kirchhoff* stress tensor[2]). Note that sufficient smoothness is assumed for W on $\mathbf{F}$. It is also useful to define the local elasticity, or tangent modulus tensor of the matrix material via

$$\mathbf{L}(\mathbf{F}) \equiv \frac{\partial^2 W}{\partial \mathbf{F}\partial \mathbf{F}}(\mathbf{F}), \quad \left(L_{ijkl}(\mathbf{F}) \equiv \frac{\partial^2 W}{\partial F_{ij}\partial F_{kl}}(\mathbf{F})\right). \tag{2.5}$$

It is further assumed that the matrix material is strongly elliptic, or *strictly* rank-one convex, namely[3]

$$B_{\mathbf{L}}(\mathbf{F}) \equiv \min_{\|\mathbf{a}\| = \|\mathbf{n}\| = 1} \{a_i n_j L_{ijkl}(\mathbf{F}) a_k n_l\} > 0. \tag{2.6}$$

The physical meaning of the above requirement is that the material never admits solutions with discontinuous deformation gradients within the given phase.

Following Hill (1972), under the above-mentioned *separation of length scales* hypothesis, the *effective stored-energy function* $\widetilde{W}$ of the inclusion-reinforced elastomer is defined by[4]

$$\widetilde{W}(\overline{\mathbf{F}}) \equiv \min_{\mathbf{F}\in\mathcal{K}(\overline{\mathbf{F}})} \langle W(\mathbf{X};\mathbf{F}) \rangle, \tag{2.7}$$

where $\mathcal{K}$ denotes the set of admissible deformation gradients,

$$\mathcal{K}(\overline{\mathbf{F}}) = \{\mathbf{F} | F_{ij} = \partial x_i(\mathbf{X})/\partial X_j \text{ for } \mathbf{X} \in \Omega_0, x_i = \overline{F}_{ij} X_j \text{ for } \mathbf{X} \in \partial\Omega_0\}.$$

Note that $\widetilde{W}$ represents the minimum elastic energy stored in the entire RVE when subjected to an affine displacement boundary condition that is consistent with the *average deformation* condition $\langle \mathbf{F} \rangle = \overline{\mathbf{F}}$. Moreover, from the definition (2.7) and the objectivity of W, it can be shown that $\widetilde{W}$ is objective. It is also noted for later reference that $\widetilde{W}$ is quasi-convex, and therefore, rank-one convex, but not necessarily strictly so, as discussed later.

Consequently, the global or macroscopic constitutive relation for the inclusion-reinforced solid can be shown to be

$$\overline{\mathbf{S}} = \frac{\partial \widetilde{W}}{\partial \overline{\mathbf{F}}} \equiv \widetilde{\mathbf{S}}. \tag{2.8}$$

where $\overline{\mathbf{S}} = \langle \mathbf{S} \rangle$ is the *average stress* in the inclusion-reinforced elastomer and $\widetilde{\mathbf{S}}$ is defined to be the *effective stress*. From here on, both $\langle \mathbf{f} \rangle$ and $\overline{\mathbf{f}}$ notations for the average of a field quantity $\mathbf{f}$ are employed interchangeably according to convenience. In analogy with the local elasticity tensor defined in (2.5), the macroscopic (or *effective*) elasticity tensor is defined

$$\widetilde{\mathbf{L}}(\overline{\mathbf{F}}) \equiv \frac{\partial^2 \widetilde{W}}{\partial \overline{\mathbf{F}}\partial \overline{\mathbf{F}}}(\overline{\mathbf{F}}), \tag{2.9}$$

where unlike the stress case in (2.8), $\widetilde{\mathbf{L}} \neq \overline{\mathbf{L}}$.

The macroscopic stability of the solid at $\overline{\mathbf{F}}$ is measured by the *effective coercivity* constant $\widetilde{B}(\overline{\mathbf{F}})$, which is defined, in terms of $\widetilde{\mathbf{L}}(\overline{\mathbf{F}})$, in an analogous way to its local counterpart (2.6), by

$$\widetilde{B}(\overline{\mathbf{F}}) \equiv \min_{\|\mathbf{a}\| = \|\mathbf{n}\| = 1} \{a_i n_j \widetilde{L}_{ijkl}(\overline{\mathbf{F}}) a_k n_l\}. \tag{2.10}$$

According to (2.10), the inclusion-reinforced solid is defined to be *macroscopically stable* if $\widetilde{B}(\overline{\mathbf{F}}) > 0$, i.e., if it is *strictly* rank-one convex. One of the issues of interest in this work is under what conditions it can lose *strict* rank-one convexity.

2.2. Microscopic instabilities in periodic inclusion-reinforced elastomers

Consider an inclusion-reinforced elastomer whose periodic, undeformed, stress-free state is used as the reference configuration. Without loss of generality, the inclusion-reinforced solid can be thought as resulting by periodic repetition

[2] The definitions of stress measures adopted follow Malvern (1969).

[3] Einstein's summation convention is adopted with repeated Latin indices summed from 1 to 3 in this section which deals with three-dimensional solids.

[4] Here and subsequently the symbol $(\widetilde{\mathbf{f}})$ implies effective properties associated with the field quantity $\mathbf{f}$, as opposed to the symbol $(\overline{\mathbf{f}})$ which implies average properties associated with the same field.

along each coordinate direction of a fundamental building block D (with boundary ∂D), which is termed the *unit cell*. Without loss of generality D is assumed to be a parallelepiped of dimension L_i along the direction X_i. Then, the distribution of the material is characterized by a $D-$periodic characteristic function:

$$\chi_0(X_1,X_2,X_3)=\chi_0(X_1+k_1L_1,X_2+k_2L_2,X_3+k_3L_3), \tag{2.11}$$

where k_1, k_2, k_3 are arbitrary integers, and L_1, L_2, L_3, the unit cell dimensions.

An objective of this work is to determine the macroscopic properties of the inclusion-reinforced solid and the stability information they carry. For hyperelastic inclusion-reinforced solids with periodic microstructure, it is known (Braides, 1985; Müller, 1987) that the computation of the effective stored-energy function $\widetilde{W}$, as determined by relation (2.7), cannot be simplified further, as a consequence of the lack of convexity of the local stored-energy function W. Recall that, for a periodic medium, the computation of the effective stored-energy function $\widetilde{W}$, as determined by relation (2.7), can be reduced to a computation on the unit cell, provided that the local stored-energy function W be convex (Marcellini, 1978). Unfortunately, actual elastomers do not have convex energy functions. However, as will be discussed in further detail below, it is still useful in this context to define the *one-cell effective energy* function $\widehat{W}$ via the expression:

$$\widehat{W}(\overline{\mathbf{F}})\equiv\min_{\mathbf{u}'\in D_{\#}}\left\{\frac{1}{|D|}\int_D W(\mathbf{X};\overline{\mathbf{F}}+\mathbf{u}'\nabla)\,d\mathbf{X}\right\}, \tag{2.12}$$

where by $D_{\#}$ is denoted the set of all D-periodic fluctuation functions $\mathbf{u}'$, i.e., zero-average displacement functions that have the same values on opposite faces of the unit cell D. Since the macroscopic deformation gradient is given by $\overline{\mathbf{F}}$, the local fluctuation field is $u'_i=u_i+X_i-\overline{F}_{ij}X_j$. Attention is focused only on macroscopic deformations $\overline{\mathbf{F}}$ for which such a fluctuation field, denoted by $\mathbf{u}'_{\overline{F}}$, exists and corresponds to a stable equilibrium solution of the unit-cell deformation problem:

$$\int_D \frac{\partial W}{\partial F_{ij}}(\mathbf{X};\overline{\mathbf{F}}+\mathbf{u}'_{\overline{F}}\nabla)\delta u_{i,j}\,d\mathbf{X}=0, \tag{2.13}$$

$$\beta_D\equiv\min_{\mathbf{u}'\in D_{\#}}\left\{\int_D \frac{\partial^2 W}{\partial F_{ij}\partial F_{kl}}(\mathbf{X};\overline{\mathbf{F}}+\mathbf{u}'_{\overline{F}}\nabla)u'_{i,j}u'_{k,l}\,d\mathbf{X}\Big/\int_D u'_{i,j}u'_{i,j}\,d\mathbf{X}\right\}>0, \tag{2.14}$$

where $\delta\mathbf{u}$ is any arbitrary D-periodic fluctuation field. The first of the above equations indicates that $\mathbf{u}'_{\overline{F}}$ is an extremum of the unit-cell energy $\widehat{W}(\overline{\mathbf{F}})$, and the second that it corresponds to a local minimum of this energy.

Although according to (2.6) the material is at each point strictly rank-one convex, this property does not usually hold for the homogenized inclusion-reinforced solid (see Abeyaratne and Triantafyllidis, 1984). The search for the macroscopic deformations $\overline{\mathbf{F}}$ for which the homogenized solid characterized by $\widehat{W}(\overline{\mathbf{F}})$ loses its strict rank-one convexity is addressed next. To this end, one needs to investigate the one-cell homogenized moduli tensor $\widehat{\mathbf{L}}(\overline{\mathbf{F}})$, defined by

$$\widehat{\mathbf{L}}(\overline{\mathbf{F}})\equiv\frac{\partial^2\widehat{W}}{\partial\overline{\mathbf{F}}\partial\overline{\mathbf{F}}}(\overline{\mathbf{F}}),\quad \widehat{W}(\overline{\mathbf{F}})=\frac{1}{|D|}\int_D W(\mathbf{X};\overline{\mathbf{F}}+\mathbf{u}'_{\overline{F}}\nabla)\,d\mathbf{X}. \tag{2.15}$$

When an explicit expression for $\widehat{W}$ exists, the homogenized moduli are calculated by taking the second derivative with respect to $\overline{\mathbf{F}}$ of $\widehat{W}$ given in (2.15). For the case of regular microgeometries where the unit-cell problem — as defined in (2.13) — is solved numerically using an F.E.M. technique, a different calculation strategy, which is based on the interchange between the homogenization and linearization steps, is employed.

Thus, for a solid with a linearized response characterized by its tangent moduli $\mathbf{L}(\mathbf{X})$, where $\mathbf{L}$ is a D-periodic function of $\mathbf{X}$, the homogenized tangent modulus tensor $\mathbf{L}^H$ is uniquely defined by (see Geymonat et al., 1993)

$$G_{ij}L^H_{ijkl}G_{kl}\equiv\min_{\mathbf{u}'\in D_{\#}}\left\{\frac{1}{|D|}\int_D L_{ijkl}(\mathbf{X})(G_{ij}+u'_{i,j})(G_{kl}+u'_{k,l})\,d\mathbf{X}\right\}, \tag{2.16}$$

where $\mathbf{G}$ is an arbitrary second-order tensor. It follows from (2.16) that the components of the homogenized tangent moduli are given by

$$L^H_{pqrs}=\frac{1}{|D|}\int_D L_{ijkl}(\mathbf{X})(\delta_{ip}\delta_{jq}+\overset{pq}{\chi}_{i,j})(\delta_{kr}\delta_{ls}+\overset{rs}{\chi}_{k,l})\,d\mathbf{X}, \tag{2.17}$$

where the characteristic functions $\overset{pq}{\boldsymbol{\chi}}\in D_{\#}$ are D-periodic fluctuations defined by

$$\int_D L_{ijkl}(\mathbf{X})(\delta_{ip}\delta_{jq}+\overset{pq}{\chi}_{i,j})\delta u_{k,l}\,d\mathbf{X}=0, \tag{2.18}$$

for arbitrary fluctuations $\delta\mathbf{u}\in D_{\#}$. A formal calculation of $\widehat{\mathbf{L}}$ based on (2.15), which makes use of (2.13), shows that (see Geymonat et al., 1993) the above-defined linearization and homogenization operations commute, and therefore

$$\widehat{\mathbf{L}}=\mathbf{L}^H. \tag{2.19}$$

It also follows from the same calculations that the characteristic functions $\overset{pq}{\boldsymbol{\chi}}$ (defined in (2.18)) involved in the determination of $\mathbf{L}^H$ are the $\overline{\mathbf{F}}$ derivatives of the fluctuation functions $\mathbf{u}'_{\overline{F}}$, namely

$$\overset{pq}{\boldsymbol{\chi}} = \frac{\partial \mathbf{u}'_{\overline{F}}}{\partial \overline{F}_{pq}}. \tag{2.20}$$

By definition, the one-cell homogenized energy $\widehat{W}$ requires minimization of the energy over a single unit cell. However, it is possible that by minimizing the energy over larger domains containing several unit cells, a lower value can be found for the energy per volume of these larger samples. The corresponding fluctuation fields are periodic over much larger (possibly infinite) domains $\mathbf{k}D$, where $\mathbf{k}D$ denotes a *super-cell* of dimensions $k_i L_i$ in each direction. Hence, a fully consistent definition (see Müller, 1987) of the homogenized energy $\widetilde{W}$ requires the consideration of fluctuations $\mathbf{u}'$ that are $\mathbf{k}D-$periodic. Thus, for a periodic hyperelastic medium, the general expression (2.7) specializes to

$$\widetilde{W}(\overline{\mathbf{F}}) \equiv \inf_{\mathbf{k}\in N^3}\left\{\min_{\mathbf{u}'\in \mathbf{k}D_{\#}}\left\{\frac{1}{|\mathbf{k}D|}\int_{\mathbf{k}D} W(\mathbf{X};\overline{\mathbf{F}}+\mathbf{u}'\nabla)\,d\mathbf{X}\right\}\right\}. \tag{2.21}$$

From the definitions in (2.12) and (2.21), one can easily conclude that $\widetilde{W}(\overline{\mathbf{F}}) \le \widehat{W}(\overline{\mathbf{F}})$. The equality holds when the infimum is a minimum occurring at $\mathbf{k}=(1,1,1)$, i.e., when the one-cell minimizing fluctuation displacement $\mathbf{u}'_{\overline{F}}$ is also the minimizing fluctuation displacement for any super-cell $\mathbf{k}D$.

For small strains (near $\overline{\mathbf{F}}=\mathbf{I}$), one expects that $\widetilde{W}(\overline{\mathbf{F}})=\widehat{W}(\overline{\mathbf{F}})$, but as the macroscopic strain increases, eventually, $\widetilde{W}(\overline{\mathbf{F}})<\widehat{W}(\overline{\mathbf{F}})$. It is always possible to calculate, exactly as well as approximately, the one-cell homogenized energy $\widehat{W}(\overline{\mathbf{F}})$ and the corresponding macroscopic moduli $\widehat{\mathbf{L}}(\overline{\mathbf{F}})$. However, it is practically impossible to calculate the correct homogenized energy $\widetilde{W}(\overline{\mathbf{F}})$, in view of the infinity of the required domain of its definition ($\mathbf{k}D$ with $\|\mathbf{k}\|\to\infty$). Therefore, it is important to establish the region of macroscopic strain space where the one-cell homogenized energy is the correct one ($\widehat{W}(\overline{\mathbf{F}})=\widetilde{W}(\overline{\mathbf{F}})$). To this end, and in an analogous way to (2.14), one can define the coercivity constant $\beta(\overline{\mathbf{F}})$ for the infinite domain ($\Omega_0=R^3$):

$$\beta(\overline{\mathbf{F}}) \equiv \inf_{\mathbf{k}\in N^3}\beta_{\mathbf{k}D}(\overline{\mathbf{F}}),$$

$$\beta_{\mathbf{k}D}(\overline{\mathbf{F}}) \equiv \min_{\mathbf{u}'\in \mathbf{k}D_{\#}}\left\{\int_{\mathbf{k}D}\frac{\partial^2 W}{\partial F_{ij}\partial F_{kl}}(\mathbf{X};\overline{\mathbf{F}}+\mathbf{u}'_{\overline{F}}\nabla)u'_{i,j}u'_{k,l}\,d\mathbf{X}\Big/\int_{\mathbf{k}D}u'_{i,j}u'_{i,j}\,d\mathbf{X}\right\}. \tag{2.22}$$

As shown by Geymonat et al. (1993), a necessary condition for $\widetilde{W}(\overline{\mathbf{F}})=\widehat{W}(\overline{\mathbf{F}})$ is that $\beta(\overline{\mathbf{F}})>0$. Fortunately, unlike the computation of $\widetilde{W}(\overline{\mathbf{F}})$, the determination of the coercivity constant $\beta(\overline{\mathbf{F}})$ requires only calculations on the unit cell D, as will be seen next. Thus, using the Bloch-wave representation theorem, it was proved by Geymonat et al. (1993) that the eigenmode $\mathbf{v}$ corresponding to $\beta(\overline{\mathbf{F}})$ can always be put in the form

$$\mathbf{v}(\mathbf{X})=\mathbf{u}'(\mathbf{X})\exp(i\omega_k X_k),\ \ \mathbf{u}'\in D_{\#},\quad \boldsymbol{\omega}\equiv(\omega_1,\omega_2,\omega_3),\ \ 0\le\omega_1 L_1,\omega_2 L_2,\omega_3 L_3<2\pi, \tag{2.23}$$

and hence that the coercivity constant $\beta(\overline{\mathbf{F}})$ is determined from

$$\beta(\overline{\mathbf{F}}) \equiv \inf_{\boldsymbol{\omega}}\left\{\min_{\mathbf{u}'\in D_{\#}}\left\{\int_D\frac{\partial^2 W}{\partial F_{ij}\partial F_{kl}}(\mathbf{X};\overline{\mathbf{F}}+\mathbf{u}'_{\overline{F}}\nabla)v^{\star}_{i,j}v_{k,l}\,d\mathbf{X}\Big/\int_D v^{\star}_{i,j}v_{i,j}.\,d\mathbf{X}\right\}\right\}, \tag{2.24}$$

with $\mathbf{v}$ given by $(2.23)_1$. Here, $\mathbf{v}^{\star}$ is the complex conjugate of the field $\mathbf{v}$.

The Euler–Lagrange equations and inclusion-matrix interface conditions corresponding to the above eigenvalue problem (2.24) are

$$(L_{ijkl}(\mathbf{X};\overline{\mathbf{F}}+\mathbf{u}'_{\overline{F}}\nabla)v_{k,l}-\beta(\overline{\mathbf{F}})v_{i,j})_{,j}=0,\quad [\![\,L_{ijkl}(\mathbf{X};\overline{\mathbf{F}}+\mathbf{u}'_{\overline{F}}\nabla)v_{k,l}-\beta(\overline{\mathbf{F}})v_{i,j}\,]\!]N_j=0, \tag{2.25}$$

where $\mathbf{N}$ is the outward normal to the inclusion-matrix interface, $[\![\,f\,]\!]$ denotes jump of the field quantity f across this interface and the eigenmode $\mathbf{v}$ is given in terms of the Bloch representation theorem (2.23). Of course, the same equations are applicable for the eigenmode corresponding to $\beta_{\mathbf{k}D}$, defined in (2.22), and also for the eigenmode corresponding to β_D, defined in (2.14).

Of particular interest here is $\beta_0(\overline{\mathbf{F}})$, the long-wavelength limit ($\boldsymbol{\omega}\to 0$) of the above expression (2.24), defined as

$$\beta_0(\overline{\mathbf{F}}) \equiv \liminf_{\boldsymbol{\omega}\to\mathbf{0}}\left\{\min_{\mathbf{u}'\in D_{\#}}\left\{\int_D\frac{\partial^2 W}{\partial F_{ij}\partial F_{kl}}(\mathbf{X};\overline{\mathbf{F}}+\mathbf{u}'_{\overline{F}}\nabla)v^{\star}_{i,j}v_{k,l}\,d\mathbf{X}\Big/\int_D v^{\star}_{i,j}v_{i,j}.\,d\mathbf{X}\right\}\right\}, \tag{2.26}$$

which, as will be subsequently discussed, when it vanishes, signals the loss of strict rank-one convexity of the one-cell homogenized stored energy $\widehat{W}(\overline{\mathbf{F}})$.

The use of $\liminf_{\boldsymbol{\omega}\to\mathbf{0}}$ in the above expression merits further explanation. As can be deduced from (2.23), two different types of eigenmodes are possible in the neighborhood of $\boldsymbol{\omega}=\mathbf{0}$; the strictly D-periodic ones, for which $\boldsymbol{\omega}=\mathbf{0}$, and the long-wavelength modes, for which $\boldsymbol{\omega}\to\mathbf{0}$. The lowest value of the ratio of the two quadratic functionals in (2.26) can occur for long-wavelength modes, in which case the limit $\boldsymbol{\omega}\to\mathbf{0}$ is a singular one depending on the ratio of the $\boldsymbol{\omega}$ components, thus justifying the use of the lim inf in (2.26).

Finally, and in analogy to the effective coercivity constant defined in (2.10), a macroscopic one-cell coercivity constant $\widehat{B}$ is defined by

$$\widehat{B}(\overline{\mathbf{F}}) \equiv \min_{\|\mathbf{a}\| = \|\mathbf{n}\| = 1} \{a_i n_j \widehat{L}_{ijkl}(\overline{\mathbf{F}}) a_k n_l\}. \tag{2.27}$$

With the definition of the three coercivity (also, and equivalently, termed *stability constants*), $\widehat{B}(\overline{\mathbf{F}})$, $\beta_0(\overline{\mathbf{F}})$ and $\beta(\overline{\mathbf{F}})$, for the macroscopic loading $\overline{\mathbf{F}}$, the stage has been set for discussing the stability of the periodic inclusion-reinforced solid at that load level. It follows from the definitions of these three coercivity constants (see Geymonat et al., 1993) that the following relation holds for arbitrary vectors $\mathbf{a}$ and $\mathbf{n}$:

$$a_i n_j \widehat{L}_{ijkl}(\overline{\mathbf{F}}) a_k n_l \geq \beta_0(\overline{\mathbf{F}}) \|\mathbf{a}\|^2 \|\mathbf{n}\|^2 \geq \beta(\overline{\mathbf{F}}) \|\mathbf{a}\|^2 \|\mathbf{n}\|^2 \implies \widehat{B}(\overline{\mathbf{F}}) \geq \beta_0(\overline{\mathbf{F}}) \geq \beta(\overline{\mathbf{F}}). \tag{2.28}$$

More specifically, the above relations indicate that when the one-cell based homogenized energy is the correct one (i.e., $\beta(\overline{\mathbf{F}}) > 0$ in which case $\widetilde{W}(\overline{\mathbf{F}}) = \widehat{W}(\overline{\mathbf{F}})$), the homogenized energy function is *strictly* rank-one convex. Moreover, microscopic stability ($\beta(\overline{\mathbf{F}}) > 0$, which means from (2.26) that the solid is stable to bounded perturbations of arbitrary wavelength $\boldsymbol{\omega}$) implies macroscopic stability ($\widehat{B}(\overline{\mathbf{F}}) > 0$, which means that the corresponding one-cell based homogenized moduli $\widehat{\mathbf{L}}$ are also strongly elliptic).

Finding the domain in macroscopic strain ($\overline{\mathbf{F}}$) space for which the material is microscopically stable, i.e., $\beta(\overline{\mathbf{F}}) > 0$, although feasible thanks to (2.24), requires tedious and time consuming calculations since one has to scan using a fine grid the $(0,2\pi) \times (0,2\pi) \times (0,2\pi)$ domain in Fourier ($\boldsymbol{\omega}$) space. On the other hand, finding the larger domain in the same macroscopic strain ($\overline{\mathbf{F}}$) space for which the one-cell homogenized solid $\widehat{W}(\overline{\mathbf{F}})$ is macroscopically stable, i.e., $\widehat{B}(\overline{\mathbf{F}}) > 0$, is a rather straightforward calculation since it only requires the determination of the homogenized moduli $\widehat{\mathbf{L}}(\overline{\mathbf{F}})$ at each macroscopic deformation $\overline{\mathbf{F}}$. Calculating these two (i.e., the microscopic and macroscopic) stability domains for certain nonlinear solids with different inclusion-reinforced microstructures is the object of the present work.

An interesting observation about the loss of macroscopic stability is in order, before ending this subsection. It has been shown by Geymonat et al. (1993) that $\widehat{B}(\overline{\mathbf{F}})$ and $\beta_0(\overline{\mathbf{F}})$ always vanish simultaneously, i.e., if $\beta_0(\overline{\mathbf{F}}) = 0$, then it implies that $\widehat{B}(\overline{\mathbf{F}}) = 0$. This means from (2.28) that the onset of a long-wavelength instability ($\boldsymbol{\omega} \to \mathbf{0}$ — the wavelength of the eigenmode is much larger compared to the unit cell size) is always detectable as a loss of strong ellipticity of the one-cell homogenized moduli. Therefore, the following remark can be made about the first — in a monotonic loading process which will be defined subsequently — loss of microscopic stability ($\beta(\overline{\mathbf{F}}_c) = 0$) in a microstructured elastic solid at some critical macroscopic deformation $\overline{\mathbf{F}}_c$: if $\beta_0(\overline{\mathbf{F}}_c) = \beta(\overline{\mathbf{F}}_c)$, the wavelength of the first instability encountered is much larger than the unit cell size and hence the instability can be detected as a loss of strong ellipticity of the one-cell homogenized moduli $\widehat{\mathbf{L}}$ since $\widehat{B}(\overline{\mathbf{F}}_c) = 0$. For the case when $\beta_0(\overline{\mathbf{F}}_c) > \beta(\overline{\mathbf{F}}_c) = 0$, the first instability encountered in the loading process has a finite wavelength, and from that point on the one-cell homogenization may no longer be physically meaningful and hence $\widehat{W}$ may not provide useful information about the solid. Henceforth a tedious numerical process that follows the bifurcated equilibrium solutions is required to determine the response of the solid under the macroscopic strains in the neighborhood of $\overline{\mathbf{F}}_c$ and beyond.

2.3. Onset-of-failure surfaces

To summarize the discussion in the two previous subsections, the elastomer's macroscopic stability constant $B(\overline{\mathbf{F}})$ is defined for the different microgeometries as follows:

$$B(\overline{\mathbf{F}}) \equiv \begin{cases} \widetilde{B}(\overline{\mathbf{F}}) \text{ random} & (\widetilde{\mathbf{L}}(\overline{\mathbf{F}}) = \partial^2 \widetilde{W} / \partial \overline{\mathbf{F}} \partial \overline{\mathbf{F}} \text{ S.O.H. only}), \\ \widehat{B}(\overline{\mathbf{F}}) \text{ periodic} & (\widehat{\mathbf{L}}(\overline{\mathbf{F}}) = \mathbf{L}^H(\overline{\mathbf{F}}) \text{ for F.E.M.}, \quad \widehat{\mathbf{L}}(\overline{\mathbf{F}}) = \partial^2 \widehat{W} / \partial \overline{\mathbf{F}} \partial \overline{\mathbf{F}} \text{ for S.O.H.}). \end{cases} \tag{2.29}$$

The top definition (see (2.10)) is employed for random microgeometries where a S.O.H. *second-order homogenization* approximation (explained in the next section) of the effective energy density $\widetilde{W}(\overline{\mathbf{F}})$ is used. The bottom definition (see (2.27)) is employed for periodic microgeometries, since a calculation of $\widetilde{W}(\overline{\mathbf{F}})$ is not feasible in this case. When a F.E.M. *finite element method* approach (also explained in the next section) is used, the one-cell homogenized moduli are calculated using $\mathbf{L}^H(\overline{\mathbf{F}})$ defined in (2.17), while for the S.O.H. approximation the one-cell homogenized moduli are obtained by differentiating $\widehat{W}(\overline{\mathbf{F}})$ (see $(2.15)_1$).

For the periodic microgeometry, the microscopic stability constant $\beta(\overline{\mathbf{F}})$ is also defined according to (2.24). The stage has thus been set to introduce the corresponding (i) *macroscopic* and (ii) *microscopic onset-of-failure surfaces* in macroscopic load space. These surfaces are, respectively, defined as the regions in macroscopic load space, where (i) $B > 0$, outside which the solid is unstable since the homogenized energy density is no longer strongly elliptic, and (ii) $\beta > 0$, inside which the infinite-cell periodic solid is stable and where the one-cell homogenization procedure is valid $\widehat{W} = \widetilde{W}$.

The parameterization of the loading path in deformation space is needed for the determination of the above-defined surfaces. A loading path $\overline{\mathbf{F}}(\lambda)$ is considered parameterized by a scalar quantity $\lambda \geq 0$, termed *load parameter*, starting at $\lambda = 0$ for $\overline{\mathbf{F}} = \mathbf{I}$, that increases monotonically with increasing applied macroscopic load. In a physically meaningful problem the solid under investigation is stable in its undeformed, stress-free state, i.e., $B(\mathbf{I}) \geq \beta(\mathbf{I}) > 0$ (initially $\overline{\mathbf{F}} = \mathbf{I}$). The macroscopic

onset-of-failure surface is thus defined by

$$B(\lambda_{cM})=0, \quad B(\lambda)>0, \ 0\le\lambda<\lambda_{cM}, \quad B(\lambda)\equiv B(\overline{\mathbf{F}}(\lambda)). \tag{2.30}$$

In other words λ_{cM} is the lowest root of $B(\lambda)$, the macroscopic stability constant defined in (2.10) and evaluated on the load path $\overline{\mathbf{F}}(\lambda)$. Similarly to (2.30), the microscopic onset-of-failure surface is given by

$$\beta(\lambda_{cm})=0, \quad \beta(\lambda)>0, \ 0\le\lambda<\lambda_{cm}, \quad \beta(\lambda)\equiv \beta(\overline{\mathbf{F}}(\lambda)). \tag{2.31}$$

In other words λ_{cm} is the lowest root of $\beta(\lambda)$, the microscopic stability constant defined in (2.24) and evaluated on the load path $\overline{\mathbf{F}}(\lambda)$. From the ordering of the stability constants in (2.28), one obtains

$$0<\lambda_{cm}\le\lambda_{cM}, \tag{2.32}$$

a property which will be used in reducing the calculations required for the microscopic onset-of-failure lines of the different composites.

The above general definition of the onset-of-failure surfaces requires the selection of a loading path. For the fiber-reinforced elastomer deformed under plane strain, of interest in this work, a proportional strain path in an appropriate macroscopic strain space will be subsequently specified.

3. Calculation methods for plane-strain loading of elastomers with cylindrical fibers

The results presented thus far are valid for three-dimensional, inclusion-reinforced elastomers with arbitrary microgeometry, macroscopic loading and rank-one convex constitutive laws. From this point on, attention is focused on plane-strain deformations (in the X_1-X_2 plane) of fiber-reinforced elastomers consisting of cylindrical fibers perpendicular to the plane of deformation and aligned in the X_3 axis direction. The fibers are taken to have initially *elliptical* cross-section and initial volume fraction f_0. All fiber sections have the same aspect ratio r, where $r\ge1$ is the ratio of the major axis of the ellipse, initially aligned with the X_1 direction, over the minor axis. Two types of fiber distributions (in the reference configuration) are considered: (a) random statistically isotropic and (b) periodic with (i) square and (ii) hexagonal arrangements as depicted in Fig. 1.

This section pertains to the load path description and to the calculation methods employed in this study. Following the description of the load paths adopted, the second subsection presents the *second-order variational estimates* used in deriving approximations for the effective properties of the fiber-reinforced elastomer. Finally the third subsection presents the main assumptions used in the *finite element method* calculations.

3.1. Loading paths

Note that the applied macroscopic deformation $\overline{\mathbf{F}}$ in this context is entirely characterized by the four in-plane components: $\overline{F}_{11},\overline{F}_{22},\overline{F}_{12},\overline{F}_{21}$, since the out-of-plane components are fixed: $\overline{F}_{13}=\overline{F}_{31}=\overline{F}_{23}=\overline{F}_{32}=0$, and $\overline{F}_{33}=1$. For convenience, the coordinates X_i defining the periodic elastomer's axes of orthotropy in the reference configuration are

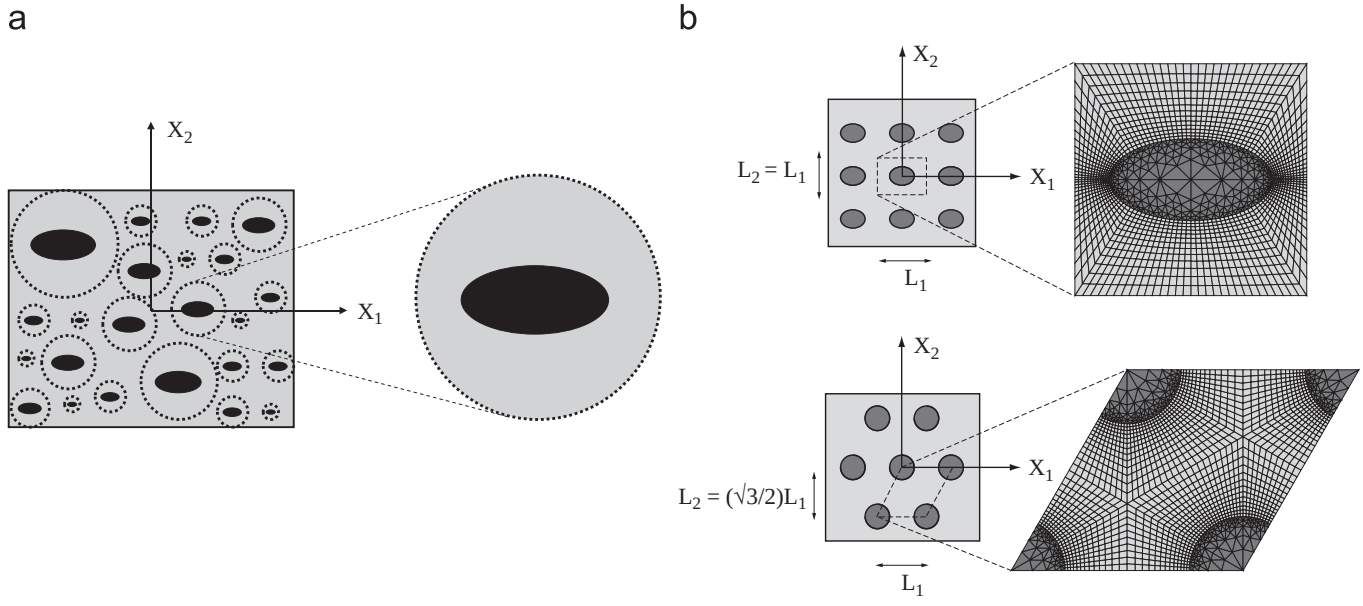

Fig. 1. Reference configuration depiction of the various microgeometries investigated: (a) random statistically isotropic and (b) perfect periodic with (i) square (top) and (ii) hexagonal (bottom) arrangement of cylindrical fibers.

identified here with the fixed laboratory frame of reference. In the sequel, the components of any tensorial quantity will be referred to X_i.[5]

Two different macroscopic loading paths are considered in strain space. The first corresponds to straining, by a different amount in each direction, along the two axes of orthotropy of the composite

$$\overline{F}_{11}=\lambda_1=\exp(\varepsilon_1),\quad \overline{F}_{12}=0,\quad \overline{F}_{21}=0,\quad \overline{F}_{22}=\lambda_2=\exp(\varepsilon_2), \tag{3.1}$$

where, λ_i denote the in-plane macroscopic principal stretches and ε_i the corresponding logarithmic strains. Loadings with $\varepsilon_1+\varepsilon_2>0$ ($\varepsilon_1+\varepsilon_2<0$) correspond to macroscopic dilation (contraction) of the composite. Within this type of macroscopic loadings, a load path needs to be selected and parameterized. Here, without loss of generality, attention is restricted to proportional straining paths in principal logarithmic strain space. More specifically, it is assumed that the ratio of the principal logarithmic strains ε_i is fixed, namely

$$\varepsilon_1=\lambda\cos\varphi,\quad \varepsilon_2=\lambda\sin\varphi. \tag{3.2}$$

where λ is the monotonically increasing *load parameter* of the process and φ is the *load path* angle.

Given the small compressibility of elastomers, it makes sense to consider loading paths that preserve macroscopic incompressibility. To this end we further consider loading paths that superimpose a shear strain γ to a zero dilation loading $\varepsilon_1+\varepsilon_2=0$, both with respect to the fixed laboratory axes. More specifically, and because of the composite's orthotropy, two generalized macroscopic shear loadings γ_{12} and γ_{21} are considered

$$\gamma_{12}:\overline{F}_{11}=\lambda_1=\exp(\varepsilon_1),\quad \overline{F}_{12}=\gamma,\quad \overline{F}_{21}=0,\quad \overline{F}_{22}=1/\lambda_1=-\exp(\varepsilon_1),$$

$$\gamma_{21}:\overline{F}_{11}=\lambda_1=\exp(\varepsilon_1),\quad \overline{F}_{12}=0,\quad \overline{F}_{21}=\gamma,\quad \overline{F}_{22}=1/\lambda_1=-\exp(\varepsilon_1), \tag{3.3}$$

A linear load path in $\varepsilon_1-\gamma$ macroscopic strain space is again chosen

$$\varepsilon_1=\lambda\cos\varphi,\quad \gamma=\lambda\sin\varphi. \tag{3.4}$$

where λ is the monotonically increasing *load parameter* of the process and φ is the *load path* angle.

The microscopic and macroscopic onset-of-failure surfaces to be computed here are found by marching along (starting from $\lambda=0$) all radial paths $\varphi\in[0,2\pi)$ in $\varepsilon_1-\varepsilon_2$ or $\varepsilon_1-\gamma_{ij}$ strain space.

3.2. Second-order variational estimates

As stated above, the determination via (2.7) of the effective stored-energy function $\widetilde{W}$ is a difficult problem, especially for fiber-reinforced elastomers with *random* microgeometry, where numerical approaches based on detailed microstructural models become infeasible. Here use will be made of the *second-order homogenization* theory (S.O.H.) of Lopez-Pamies and Ponte Castañeda (2006a) to generate estimates for $\widetilde{W}$ and its derivatives for the fiber-reinforced elastomers considered in this work.

The key concept behind the S.O.H. theory is the construction of suitable variational principles utilizing the idea of a *linear comparison composite* (L.C.C.). This homogenization technique, which is exact to second order in the heterogeneity contrast (hence its name), has the capability to incorporate statistical information about the microstructure beyond the volume fraction and can be applied to large classes of hyperelastic composites. For brevity, here only the Hashin–Shtrikman-type (HS-type) estimates specialized to elastomers reinforced with aligned cylindrical fibers are presented; see Sections 4.3 and 4.4 in Lopez-Pamies and Ponte Castañeda (2006a) for a detailed description of these results.

Thus, the HS-type second-order estimate for the effective stored-energy function of a fiber-reinforced elastomer — made of a hyperelastic matrix phase with stored-energy function $W^{(1)}$ reinforced by a random distribution of aligned hyperelastic fibers with stored-energy function $W^{(2)}$ — is given by

$$\widetilde{W}(\overline{\mathbf{F}})=(1-f_0)W^{(1)}(\widehat{\mathbf{F}}^{(1)})+S^{(1)}_{ij}(\overline{\mathbf{F}})[\overline{F}_{ij}-f_0\overline{F}^{(2)}_{ij}-(1-f_0)\widehat{F}^{(1)}_{ij}]+f_0W^{(2)}(\overline{\mathbf{F}}^{(2)}). \tag{3.5}$$

Here, $\overline{\mathbf{F}}^{(2)}$ is the average deformation gradient in the fibers and $\widehat{\mathbf{F}}^{(1)}$ is a variable that contains information about the fluctuations of the deformation gradient field in the matrix phase. They are, respectively, determined by the following nonlinear algebraic equations:

$$\overline{F}^{(2)}_{ij}=\overline{F}_{ij}-(1-f_0)P_{ijkl}[L_{klmn}(\overline{F}_{mn}-\overline{F}^{(2)}_{mn})-S^{(1)}_{kl}(\overline{\mathbf{F}})+S^{(2)}_{kl}(\overline{\mathbf{F}}^{(2)})], \tag{3.6}$$

and

$$S^{(1)}_{ij}(\widehat{\mathbf{F}}^{(1)})-S^{(1)}_{ij}(\overline{\mathbf{F}})=L_{ijkl}(\widehat{F}^{(1)}_{kl}-\overline{F}_{kl}). \tag{3.7}$$

In these expressions, $\mathbf{P}$ is an Eshelby-type tensor that contains information about the microstructure in the undeformed configuration, while $\mathbf{L}$ is the modulus tensor of the matrix phase in a suitable L.C.C. that must be obtained from certain optimality conditions. In particular, for isotropic matrix phases, the tensor $\mathbf{L}$ should be taken of the form (see Lopez-Pamies

[5] Here and subsequently, Latin indices range from 1 to 2.

and Ponte Castañeda, 2006b)

$$L_{ijkl}=\overline{Q}_{rm}\overline{Q}_{jn}\overline{Q}_{sp}\overline{Q}_{lq}\overline{R}_{ir}\overline{R}_{ks}L^*_{mnpq}, \tag{3.8}$$

where the proper orthogonal tensors $\overline{\mathbf{Q}}$ and $\overline{\mathbf{R}}$ are defined by the decomposition $\overline{\mathbf{F}}=\overline{\mathbf{R}}\,\overline{\mathbf{Q}}\,\overline{\mathbf{A}}\,\overline{\mathbf{Q}}^T$, with $\overline{A}_{ij}=\mathrm{diag}(\lambda_1,\lambda_2)$, $\mathbf{L}^*$ is orthotropic with respect to the X_i axis, with non-zero components $L^*_{1111}=\ell^*_1$, $L^*_{2222}=\ell^*_2$, $L^*_{1212}=\ell^*_3$, and $L^*_{1122}=\ell^*_4$ and where

$$L^*_{2121}=\ell^*_3 \quad \text{and} \quad L^*_{1221}=\sqrt{(\ell^*_1-\ell^*_3)(\ell^*_2-\ell^*_3)}-\ell^*_4. \tag{3.9}$$

Note that, since $\overline{\mathbf{Q}}$ and $\overline{\mathbf{R}}$ can be readily computed from the applied loading $\overline{\mathbf{F}}$, it is inferred from condition (3.9) that the modulus tensor $\mathbf{L}$ of the matrix phase in the L.C.C. contains four independent unknowns: ℓ^*_1, ℓ^*_2, ℓ^*_3, and ℓ^*_4. The optimal value of these parameters is determined by the relations

$$(\widehat{F}^{(1)}_{ij}-\overline{F}_{ij})\frac{\partial L_{ijkl}}{\partial \ell^*_\alpha}(\widehat{F}^{(1)}_{kl}-\overline{F}_{kl})=\frac{f_0}{(1-f_0)^2}(\overline{F}_{ij}-\overline{F}^{(2)}_{ij})\frac{\partial D_{ijkl}}{\partial \ell^*_\alpha}(\overline{F}_{ij}-\overline{F}^{(2)}_{ij}) \tag{3.10}$$

($\alpha=1,2,3,4$), where

$$\mathbf{D}=\mathbf{P}^{-1}-(1-f_0)\mathbf{L}. \tag{3.11}$$

At this stage, the only variable that remains to be specified is the microstructural tensor $\mathbf{P}$ that depends on the size, shape and orientation of the fibers, as well as on their spatial distribution in the reference configuration. In particular, the tensor $\mathbf{P}$ depends on whether the distribution of the fibers is *periodic* (Nemat-Nasser et al., 1982; Suquet, 1990a,b), or *random* (Willis, 1977; Ponte Castañeda and Willis, 1995). The explicit expressions for $\mathbf{P}$ for the three types of microstructures considered in this work are given in Appendix B.

In summary, Eqs. (3.6), (3.7), and (3.10) constitute a closed system of 12 coupled, nonlinear, algebraic equations for the 12 unknowns formed by the four components of $\overline{\mathbf{F}}^{(2)}$, the four components of $\widehat{\mathbf{F}}^{(1)}$, and the four independent components of $\mathbf{L}$ (denoted by ℓ^*_α). It is possible (see Lopez-Pamies and Ponte Castañeda, 2006b) to solve in *closed form* Eq. (3.10) for the components of $\widehat{\mathbf{F}}^{(1)}$ in terms of the parameters ℓ^*_α. The resulting expressions can then be substituted into Eq. (3.7) to obtain, together with (3.6), a system of eight equations for the eight unknowns $\overline{F}^{(2)}_{11}$, $\overline{F}^{(2)}_{12}$, $\overline{F}^{(2)}_{21}$, $\overline{F}^{(2)}_{22}$, ℓ^*_1, ℓ^*_2, ℓ^*_3, and ℓ^*_4, which must be solved numerically.

Having computed all the values of $\overline{\mathbf{F}}^{(2)}$ and ℓ^*_α ($\alpha=1,2,3,4$) for given matrix and fiber stored-energy functions $W^{(1)}$ and $W^{(2)}$, fiber aspect ratio r, volume fraction f_0, and spatial distribution, and loading $\overline{\mathbf{F}}$, the values of the components of $\widehat{\mathbf{F}}^{(1)}$ can be readily determined from (3.10). In turn, the second-order estimate for the effective behavior of fiber-reinforced elastomers can be computed, from relation (3.5), using these results. Finally, having determined $\widetilde{W}(\mathbf{F})$ via (3.5), it is straightforward to compute its second derivative, i.e., the macroscopic elasticity tensor $\widetilde{\mathbf{L}}(\overline{\mathbf{F}})$ according to (2.9), in order to examine the macroscopic stability of the solid via the coercivity constant $\widetilde{B}(\overline{\mathbf{F}})$ defined in (2.10).

3.3. Finite element method

In addition to the above-described, approximate, S.O.H.-based method, a more accurate *finite element method* (F.E.M.) approach is also employed to calculate the deformed configuration (i.e., to find $\mathbf{u}'_{\overline{F}}$), the one-cell homogenized moduli $\widehat{\mathbf{L}}$, as well as the microscopic λ_{cm} and macroscopic λ_{cM} onset-of-failure loads for the periodic elastomers. The details of the corresponding F.E.M. algorithm are given in Triantafyllidis et al. (2006). However, for reasons of completeness of the presentation, a brief description of this algorithm is included here.

For the matrix material discretization, the F.E.M. calculations use eight node (16 d.o.f.) quadratic interpolation, isoparametric, quadrilateral elements with a 2×2 Gaussian under-integration scheme to avoid compressibility locking. For the inclusions, the F.E.M. calculations use six node (12 d.o.f.) quadratic interpolation, isoparametric, triangular elements with a three-point Hammer under-integration scheme, again to avoid compressibility locking.

The same type of constitutive model is used both for the matrix and the fiber. However, to numerically approximate a rigid fiber, the stiffness constants describing the fiber are taken several orders of magnitude higher than their matrix counterparts. More specifically, for the F.E.M. calculations reported here, the fiber-to-matrix ratio of the initial (i.e., at zero strain) stiffnesses is taken to be $\mu_f/\mu_m\equiv\eta=10^3$. This choice ensures that the fiber sections rotate as rigid discs, as evidenced in all the F.E.M. results obtained here.

As an example of the discretization used, the unit cell for the square microgeometry with an initial fiber volume fraction $f_0=\pi/16\approx 0.2$ and a fiber section aspect ratio r=2 (see the top drawing in Fig. 1b) the mesh has 2096 elements with 5873 nodes (11,746 d.o.f). For the cell of the hexagonal microgeometry with the same initial fiber volume fraction and a circular section fiber (r=1) (see the bottom drawing in Fig. 1b) a 2112 element mesh with 5929 nodes (11,858 d.o.f.) is used. For the imperfect 3×3 cell aggregate (see Fig. 12) the mesh has 27,332 elements with 63,125 nodes (126,250 d.o.f.). This discretization is found to be more than adequate for the accuracy of the numerical calculations, since further mesh refinement does not result in appreciably different onset-of-failure curves.

The governing equations for the unit-cell deformation problem (2.13) subjected to $\mathbf{F}(\lambda)$, defined in (3.1), are solved using an incremental Newton–Raphson algorithm. A typical step size $\Delta\lambda$ of the load parameter λ, defined in (3.2), is $\Delta\lambda=10^{-2}$ for all paths. Occasionally larger step sizes are employed to shorten calculation time. For most cases three to four iterations are

required for convergence at each load step and the accuracy criterion required to stop the iterations, based on the residual nominal stress ($\mathbf{S}=\partial W/\partial \mathbf{F}$) vector's maximum component norm, is $\|\mathbf{S}\| \le 10^{-6}\|\overline{\mathbf{S}}\|$. The graphs of the microscopic and macroscopic onset-of-failure surfaces are calculated using 360 different load path angles (starting with $\varphi=0$ and repeating the calculations by increasing each time the path angle by $\Delta\varphi=\pi/180$).

Calculations, at each load λ, of the one-cell homogenized moduli tensor $\widehat{\mathbf{L}}(\lambda)(=\mathbf{L}^H(\lambda))$ are based on (2.17) and (2.18) as detailed in Triantafyllidis et al. (2006). The thus calculated tensor $\widehat{\mathbf{L}}(\lambda)$ is then used to find the macroscopic coercivity constant $\widehat{B}(\overline{\mathbf{F}}(\lambda))$ defined in (2.27) and subsequently the macroscopic onset-of-failure load λ_{cM} according to the definition (2.30). The calculation of the microscopic onset-of-failure load λ_{cm}, defined in (2.31), is based on the macroscopic coercivity constant $\beta(\overline{\mathbf{F}}(\lambda))$ and takes advantage of (2.32) to drastically reduce the required calculations.

For each loading path, the determination of the loss of macroscopic ellipticity (i.e., of λ_{cM}) is done first. Starting at λ_{cM}, the load parameter is decreased by steps of $-\Delta\lambda$. At each load level, the stability of the infinite perfect structure is investigated by scanning all wavenumbers $(\omega_1 L_1,\omega_2 L_2)\in(0,2\pi)\times(0,2\pi)$ according to the algorithm described in Triantafyllidis et al. (2006) by using a uniform 72×72 grid. If an instability is detected for a certain wavenumber $\boldsymbol{\omega}$, calculations are stopped and the load changed by an additional $-\Delta\lambda$. The procedure continues until a stable configuration is found over the entire Fourier space $(0,2\pi)\times(0,2\pi)$. A bisection method is subsequently used to accurately determine the load at the onset of first bifurcation, (i.e., of λ_{cm}).

4. Application to a representative class of fiber-reinforced elastomers

Here are presented the calculations for the in-plane deformations of rigid fiber-reinforced elastomers with different microgeometries and matrix properties. Following the description of the different matrix constitutive laws used in the calculations, the results are organized in three groups as follows. The first group, Fig. 2, pertains to the influence of microgeometry and matrix constitutive law on the macroscopic stress–strain response of the hyperelastic composite under simple shear along different directions. The second group, Figs. 3 and 4, investigates the influence of microgeometry and initial fiber volume fraction on the microscopic and macroscopic onset-of-failure curves in neo-Hookean matrix, fiber-reinforced elastomers under plane strain loading with principal directions aligned with the axes of orthotropy of the elastomer. Finally the third group, Figs. 5–14, addresses the influence of microgeometry, initial fiber volume fraction, fiber cross-section, matrix constitutive law and fiber-matrix interface strength on the microscopic and macroscopic onset-of-failure curves in fiber-reinforced elastomers under plane-strain loading paths that preserve macroscopic incompressibility.

An important general remark about the onset-of-failure curves should be made at this point. For the calculation of the first — as the load parameter λ increases along a given load path $\overline{\mathbf{F}}(\lambda)$ — microscopic (at λ_{cm}) or macroscopic (at λ_{cM}) instability to be physically meaningful, one must ensure that no other type of *failure* is encountered along the load path in question for loads lower than λ_{cm} (or lower than λ_{cM} in the case that the lower microscopic instability load λ_{cm} is not available). There are several phenomena that can signal some other (than the loss of uniqueness of the one-cell periodic solution or of the rank-one convexity) type of failure of the fiber-reinforced elastomer, and need to be taken into account. These phenomena are: (a) *cavitation*, i.e., the opening of voids in the elastomeric matrix due to the high levels of hydrostatic tension, (b) *decohesion*, due to high tensile normal stress at the fiber-matrix interface and (c) *fiber contact* which can occur under compression. A detailed discussion of these failure phenomena is presented in Appendix A.

4.1. Matrix material properties

Two different hyperelastic, strictly rank-one convex matrix materials are used here. They are distinguished by their response in simple shear, the first being linear the other reaching an asymptote at a finite strain. Their energy densities are given in terms of the following two invariants associated with $\mathbf{F}$

$$I\equiv F_{ij}F_{ij},\quad J\equiv \det(F_{ij}). \tag{4.1}$$

The first material is a compressible *neo-Hookean* solid, with strain energy $W(\mathbf{F})$

$$W=\frac{\mu}{2}[(I-2)-2\ln J]+\frac{\kappa-\mu}{2}(J-1)^2, \tag{4.2}$$

where μ and κ are, respectively, the shear and bulk moduli of the solid at zero strain. The response of this solid in simple shear is linear, with a unit slope because of the adopted non-dimensionalization for the stress.

The second material used is a compressible *Gent* solid, with strain energy $W(\mathbf{F})$ given by

$$W=-\frac{\mu}{2}\left[J_m\ln\left(1-\frac{I-2}{J_m}\right)+2\ln J\right]+\left[\frac{\kappa-\mu}{2}-\frac{\mu}{J_m}\right](J-1)^2, \tag{4.3}$$

where μ and κ have the same interpretation as in (4.2) and J_m is a constant related to the solid's strain saturation. Indeed, as expected from (4.3), the stresses become infinite as the strains (measured by the first invariant) approach J_m + 2. This asymptotic behavior is motivated by the reversible elastic range response of natural rubbers which cannot sustain strains above a certain level without failure. The numerical value J_m=50, which has been used by Michel et al. (2007) is also

adopted for all the numerical calculations reported in this work. Note that at the limit $J_m \to \infty$, the Gent energy density in (4.3) converges to the neo-Hookean energy density in (4.2).

Both neo-Hookean and Gent solids (for $\mu > 0$, $J_m > 0$, $\kappa > [(J_m+2)/J_m]\mu$) are strictly polyconvex, as defined in Ball (1977), since they are strictly convex functions of I and J, and hence strictly rank-one convex, i.e., they must satisfy (2.6). Finally, it must be pointed out that upon a linearization of the deformation gradient, the above two laws reduce to the same small strain, linearly elastic solid with shear and bulk moduli μ and κ, respectively.

4.2. Macroscopic stress–strain response

Some general remarks applicable to Fig. 2 are first in order. All composites have the same initial fiber volume fraction ($f_0 = \pi/16 \approx 0.2$) and the same stress–strain response at zero strain, since the two different matrix laws used have the same initial shear and bulk moduli ($\kappa/\mu = 10$). The calculations are done for two different initial microgeometries: (i) hexagonal and (ii) random polydisperse distributions of fibers with circular sections (aspect ratio $r=1$). For each microgeometry three different isochoric loading paths are considered. The first two are simple shear paths γ_{12} and γ_{21} described in (3.3). The third path consists of isochoric biaxial stretching, a special case of (3.1) where $\varepsilon_1 + \varepsilon_2 = 0$. The latter loading results from the superposition of two simple shear loadings, a $\gamma_{21} = \gamma/2$ and a $\gamma_{12} = \gamma/2$, plus some higher order stretching (of $(1+(\gamma/2)^2)^{1/2}$ to be exact) along each axis, where the axes of deformation are fixed but rotated by $\pi/4$ with respect to the X_i axes.

The shear stresses τ plotted in Fig. 2 are taken to be the corresponding macroscopic Cauchy stresses $\overline{\sigma}_{21}$, $\overline{\sigma}_{12}$ and $|\overline{\sigma}_{22} - \overline{\sigma}_{11}|/2$, respectively, where the latter is the shear stress at $\pi/4$ with respect to the principal directions of the isochoric biaxial stretching. The results for the periodic microgeometry are based on F.E.M. calculations (solid lines), while for the random microgeometry S.O.H. calculations (bullet-marked lines) are used. On the hexagonal microgeometry composite stress–strain curves, are also marked by solid triangles the loss of ellipticity of the corresponding homogenized moduli, the onset-of-cavitation in the matrix as well as the onset-of-decohesion, while on the corresponding curves for the random microgeometry composite the onset-of-decohesion in marked by solid squares (onset-of-cavitation cannot be calculated for the S.O.H. approximation, while the random microgeometry elastomer with circular inclusions does not loose macroscopic ellipticity). For explanations on the decohesion and cavitation calculations, see Appendix A.

For small strains all the three different loadings are simple shearing with respect to different axes. Given the isotropy of the hexagonal microgeometry composite at zero strain, as well as the isotropy of the random microgeometry composite, all three loading paths start — for either microgeometry composite and for either constitutive law, since the two matrix materials coincide at zero strain — with the same initial tangent, as seen in Fig. 2. Moreover, as expected from the isotropy

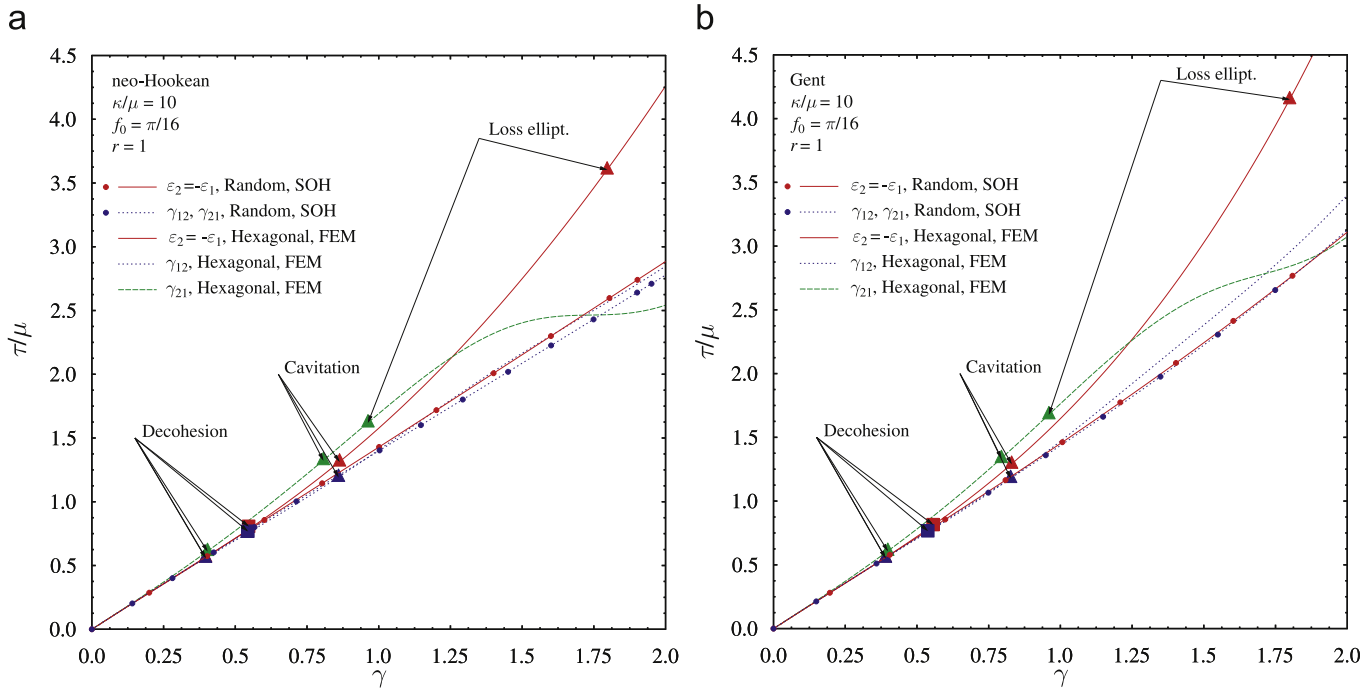

Fig. 2. Influence of microgeometry and matrix constitutive law on the macroscopic dimensionless Cauchy shear stress-shear strain response of fixed initial fiber volume fraction ($f_0 = \pi/16 \approx 0.2$) elastomers reinforced with circular section ($r=1$) fibers: (a) neo-Hookean, and (b) Gent matrix material (with same shear and bulk moduli). The composites are subjected to three different plane-strain loading paths in simple shear. For the hexagonal microgeometry, the results are based on F.E.M. calculations and are shown in solid lines, while for the random polydisperse microgeometry, the results are based on S.O.H. calculations and are shown in bullet-marked lines. Decohesion, cavitation and macroscopic loss of ellipticity are marked by solid triangles for the hexagonal microgeometry composites while decohesion for the random microgeometry composites is marked by solid squares.

of the random microgeometry composite, there is no difference in its response for the γ_{21} and γ_{12} loading paths at all strain levels.

For the hexagonal microgeometry, after a strain $\gamma \approx 0.2$, the stress–strain paths start diverging: γ_{12} has the softest (almost linear) response, γ_{21} shows initially the stiffest response while $\varepsilon_1 = -\varepsilon_2$ lies between the other two. Such a behavior is expected since the two γ_{ij} paths corresponds to shearing rotated at $\pm\pi/4$ with respect to isochoric biaxial stretching path and the hexagonal microgeometry composite is no longer isotropic at finite strains. The γ_{12} and $\varepsilon_1 = -\varepsilon_2$ paths have slopes that increase monotonically with the applied strain, while the γ_{21} path slope starts decreasing and crosses the $\varepsilon_1 = -\varepsilon_2$ path at $\gamma \approx 1.25$ and the γ_{12} path at even higher strains. This large stiffness variation of the periodic composite's stress–strain response under the γ_{21} simple shear is due to the evolution of the microstructure; particles along rows parallel to the shearing direction periodically get aligned and then misaligned, as discussed by Lahellec et al. (2004) and Brun et al. (2007). Note that because of this effect, the neo-Hookean matrix composite's slope of the stress–strain path for γ_{21} is almost zero for strains of $\gamma \in [1.6,1.8]$ approximately, as seen in Fig. 2a.

For the random, isotropic, polydisperse composite the stress–strain paths are always monotonic (almost linear) and lie below the response of the corresponding hexagonal composite. The approximate S.O.H. model predicts a somewhat stiffer response for the $\varepsilon_1 = -\varepsilon_2$ as compared to the γ_{ij} paths (the response for γ_{21} and γ_{12} is identical, due to the isotropy of the random, polydisperse composite), consistently with the F.E.M. predictions for the hexagonal composite. The differences between the $\varepsilon_1 = -\varepsilon_2$ and γ_{12} responses are small even for high strains for the neo-Hookean random composite (see Fig. 2a) and almost non-existent for the corresponding random Gent case (see Fig. 2b).

The macroscopic stress–strain response of the neo-Hookean and Gent composites are very similar, with the latter being somewhat stiffer compared to the former at higher strains as expected from the corresponding response of the two matrix materials. It is also worth noticing that up to failure by cavitation (see Appendix A), there is no discernible influence of the matrix material in the response of the composite, thus justifying the choice adopted herein to do most of the ensuing calculations for neo-Hookean matrix composites. The matrix constitutive law issue will be revisited subsequently, providing more supporting evidence for the neo-Hookean material choice, when its influence on the onset-of-failure curves is investigated in Fig. 13.

4.3. Onset-of-failure curves for neo-Hookean composites loaded along orthotropy axes

The influence of fiber volume fraction, microgeometry and matrix material compressibility on the failure curves of fiber-reinforced elastomers subjected to plane-strain loading with principal directions aligned with the axes of orthotropy of the composite, as described in (3.1) and (3.2), is presented next in Figs. 3 and 4. All results in this subsection are calculated using a neo-Hookean matrix material and fibers with circular cross-section (r=1).

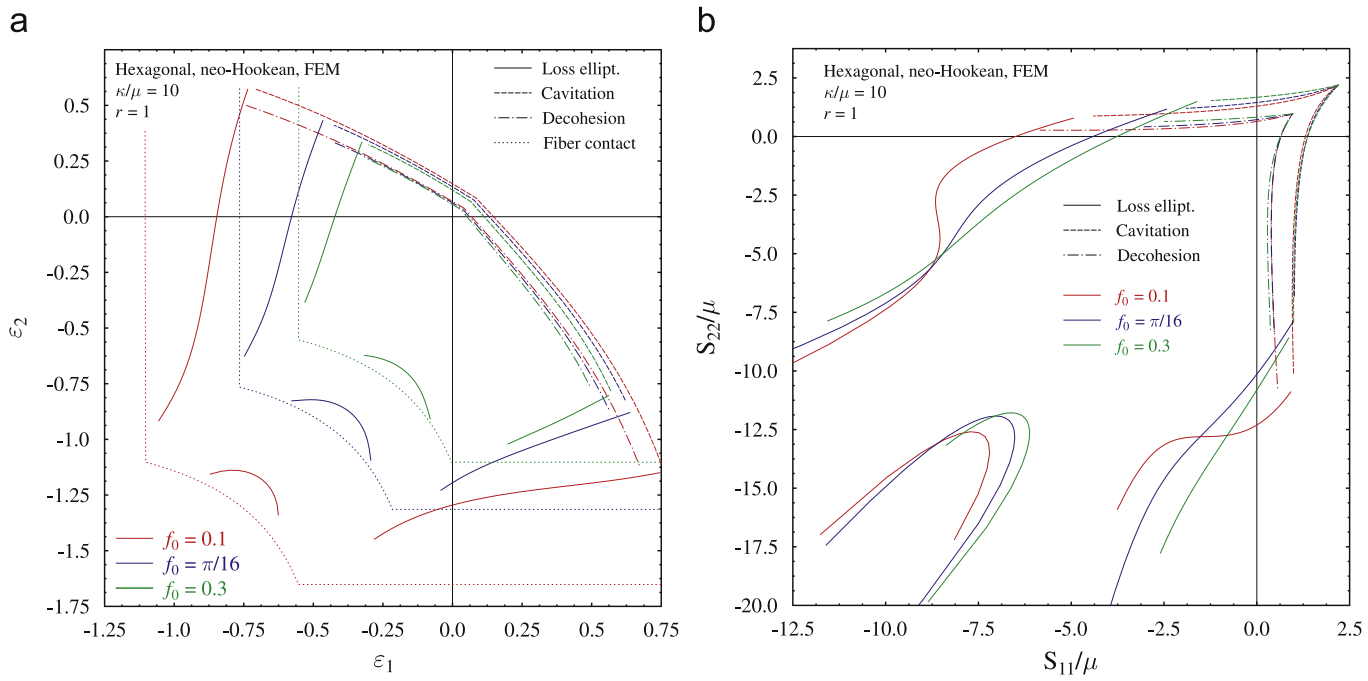

Fig. 3. Influence of initial fiber volume fraction (f_0) on the onset-of-failure curves in (a) macroscopic strain space and in (b) dimensionless macroscopic stress space for neo-Hookean matrix ($\kappa/\mu = 10$), hexagonal microgeometry composites, reinforced with circular section fibers (r=1) and loaded under plane-strain, along the X_1, X_2 directions. Macroscopic loss of ellipticity is depicted by solid lines, matrix cavitation by dashed lines, fiber decohesion by dot–dash lines and fiber contact by dotted lines. Results are based on F.E.M. calculations.

The onset-of-failure curves for the periodic hexagonal microgeometry, obtained by F.E.M. calculations, are presented in Fig. 3. More specifically, in Fig. 3a are plotted, in principal logarithmic strain space, the curves for the macroscopic onset-of-failure (loss of ellipticity of the homogenized moduli, solid lines), the onset-of-cavitation in the matrix (dashed lines), and the onset-of-decohesion at the fiber-matrix interface (dot–dash lines). The locus of strains corresponding to fiber contact, a straightforward geometric calculation, are also marked (dotted lines). The same results, plotted in dimensionless stress space — principal nominal stress over shear modulus (S_{ii}/μ) — are presented in Fig. 3b.

The macroscopic onset-of-failure curves in strain space in Fig. 3a are similar to the ones calculated by Nestorović and Triantafyllidis (2004) for the same matrix material, but for a slightly different microgeometry — diagonal, instead of the present hexagonal fiber arrangement — and for slightly different values of the material constants. The macroscopic and microscopic onset-of-failure curves are always coincident, which means that when a bifurcation type instability is encountered along a radial loading path, its characteristic wavelength is much larger than the unit cell size.

There are two loading zones in biaxial contraction along which no bifurcation instability is detected prior to fiber contact. These zones are centered about the hydrostatic compression of the composite during which the fibers approach each other at the same rate. The corresponding deformation paths, found from geometric considerations when three adjacent fibers are equidistant, are $\varepsilon_1=\varepsilon_2$ and $\varepsilon_1=\varepsilon_2+0.5\ln(3)$ and are easily visualized by joining the corresponding corner points of the different f_0 fiber contact curves in Fig. 3a. For paths about the hydrostatic compression loading of the (initially isotropic) hexagonal microgeometry composite, the principal (unit-cell-periodic) solution is found to be stable all the way up to fiber contact. One possible explanation is the (almost) isotropic hydrostatic compression of the circular section fiber, hexagonal composite is not that different from the corresponding deformed state of its random, polydisperse counterpart which has been shown to never lose ellipticity (Lopez-Pamies and Ponte Castañeda, 2006b).

Notice the absence of bifurcation type instabilities in the biaxial extension zone and in parts of the mixed loading quadrants (i.e., $\varepsilon_1\varepsilon_2<0$), roughly above the simple shear line $\varepsilon_1=-\varepsilon_2$, in the deformation region which corresponds to a macroscopic dilation of the composite ($\varepsilon_1+\varepsilon_2>0$). The composite's overall dilation implies dilation of the compressible matrix, thus leading to cavitation. Prior to cavitation the maximum normal stress at the fiber/matrix interface reaches the magnitude of the shear modulus, thus signaling decohesion, according to the definition adopted ($\delta_c\equiv(\sigma_{nn}/\mu)_{max}=1$, see Appendix A). Decohesion always precedes cavitation along each radial path and both these phenomena occur at macroscopic strains at least an order of magnitude lower than the strains for the onset of the macroscopic loss of ellipticity of the composite.

As the initial fiber volume fraction f_0 increases, the macroscopic loss of ellipticity occurs at lower macroscopic strains and the corresponding curves recede towards the origin while keeping the same overall shape. The decrease of macroscopic instability strains for higher fiber volume fractions is expected, since instability is driven by compressive stresses in the ligaments; as the ligaments become thinner with increasing fiber volume fractions, the same compressive stress levels are reached for lower overall macroscopic strains and instabilities occur earlier. However, unlike the loss of ellipticity instabilities which dominate the contraction part of the macroscopic strain space, the decohesion and cavitation instabilities occurring in the dilation part of the same space depend on the local stress fields reaching a critical value and hence are relatively insensitive to the initial fiber volume fraction.

The results of the same calculations are plotted in macroscopic, dimensionless principal stress space in Fig. 3b. Unlike the strain plot in Fig. 3a, the macroscopic stresses corresponding to the onset of macroscopic loss of ellipticity are not increasing monotonically with the initial fiber volume fraction, neither do the corresponding stresses vary as much. The critical macroscopic stresses for the onset-of-cavitation and decohesion are, for the reason previously explained, almost insensitive to f_0. Notice that no fiber contact curves are shown in Fig. 3b, since the corresponding stresses are infinitely large.

Calculations reported in Fig. 4a correspond to the same composites as in Fig. 3a, except that here the composite has a square, instead of a hexagonal, microgeometry. The same line drawing convention as Fig. 3a is used here for plotting the different onset-of-failure curves. Moreover, and in addition to the F.E.M. results (solid lines), results from S.O.H. calculations for the same composites are also presented (bullet-marked lines).

Again, the macroscopic onset-of-failure curves in strain space are very similar to the ones calculated by Nestorović and Triantafyllidis (2004) for the same microgeometry and matrix material, but for slightly different values of the material constants. Roughly speaking and similarly to the hexagonal microgeometry, a long-wavelength bifurcation is the first instability encountered under macroscopic contraction ($\varepsilon_1+\varepsilon_2<0$), while a decohesion, followed by a cavitation are the instabilities encountered under macroscopic dilation ($\varepsilon_1+\varepsilon_2>0$). The strains for the loss of ellipticity are, once again, an order of magnitude higher than the strains at decohesion and cavitation. However, unlike the hexagonal microgeometry, for square microgeometries a macroscopic loss of ellipticity always occurs along loading paths in biaxial compression before reaching fiber contact. The reasons for the decrease in critical strains with increasing initial fiber volume fraction in the macroscopic contraction part of the strain space and the corresponding insensitivity of the decohesion and cavitation curves in the macroscopic dilation part of the strain space, have already been explained in discussing Fig. 3a.

The S.O.H. predictions for cavitation[6] and loss of ellipticity are qualitatively consistent with the corresponding F.E.M. results. Thus, cavitation is observed in the dilation region and loss of ellipticity in the contraction region. The S.O.H.

[6] While no information of the local deformation can be computed with the S.O.H, the average deformation gradient in the matrix phase can be readily computed. The S.O.H. cavitation predictions in Fig. 4 are based on such an average measure.

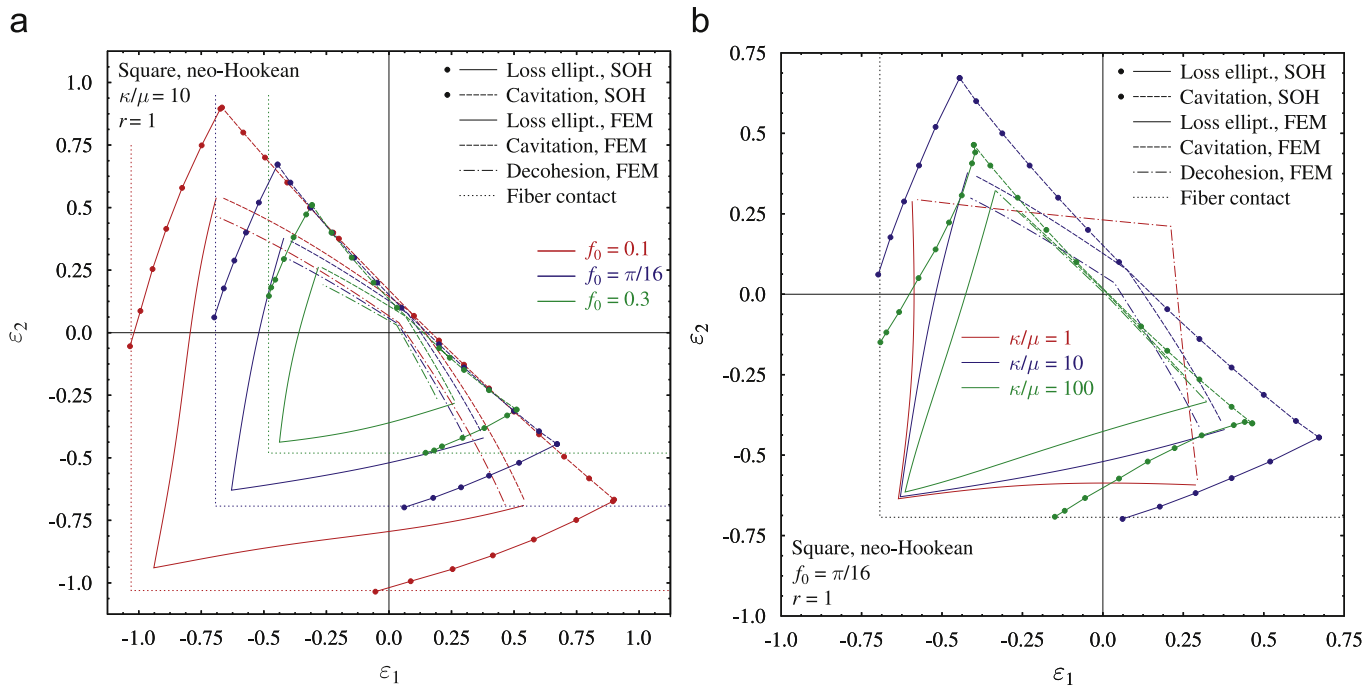

Fig. 4. Influence of (a) initial fiber volume fraction (f_0) and (b) matrix compressibility (κ/μ) on the onset-of-failure curves in macroscopic strain space for neo-Hookean matrix, square microgeometry composites, reinforced with circular section fibers (r=1) and loaded under plane-strain, along the X_1, X_2 directions. Macroscopic loss of ellipticity is depicted by solid lines, matrix cavitation by dashed lines, fiber decohesion by dot–dash lines and fiber contact by dotted lines. Results based on F.E.M. calculations are shown in solid lines while results based on S.O.H. calculations are shown in bullet-marked lines.

predictions agree remarkably well with the F.E.M. calculations in the macroscopic dilation region, where results are insensitive to f_0. However, the S.O.H. predictions for loss of ellipticity under contraction conditions are much delayed (i.e., they correspond to much larger strains) compared to the corresponding F.E.M. results — so much so that fiber contact takes place before the loss of ellipticity predicted by the S.O.H. when the loading is sufficiently close to the hydrostatic compression axes. This deficiency with the S.O.H. predictions — which gets worse with increasing volume fraction — can be attributed at least in part to the lack of accuracy of the Hashin–Shtrikman-type estimates used for the linear comparison composite. Such estimates can handle only approximately interaction effects among the fibers through two-point interactions, which are insufficient to model accurately strongly nonlinear phenomena such as those occurring when the fibers start getting close to each other; note that under highly compressive conditions the composite starts behaving as a composite with a high concentration of fibers.

All calculations reported thus far, correspond to neo-Hookean matrix composites with a compressibility ratio $\kappa/\mu=10$. The influence of matrix material compressibility on the onset-of-failure curves for the square microgeometry composite with circular section fibers (r=1) and an initial fiber volume fraction ($f_0=\pi/16\approx 0.2$) is presented in Fig. 4b. As expected, results are similar to the ones presented in Fig. 4a, with the first failure encountered in the macroscopic contraction region being a macroscopic loss of ellipticity and a decohesion followed by cavitation being the failures encountered in the macroscopic dilation region of the strain space. As the matrix material incompressibility increases, the stable region of the composite shrinks in strain space; the loss of ellipticity curves become sharper V's — all anchored about the loss of ellipticity point for hydrostatic compression at approximately $(-0.63,\ -0.63)$ — while the onset-of-cavitation curves approach the zero macroscopic dilation line ($\varepsilon_1+\varepsilon_2=0$). For the most compressible neo-Hookean matrix material ($\kappa/\mu=1$), the criterion of Lopez-Pamies (2009) does not predict cavitation and only a decohesion line exists. Notice also that the S.O.H. predictions are best for the most incompressible matrix material ($\kappa/\mu=100$) and deteriorate with increasing matrix compressibility. For the most compressible case ($\kappa/\mu=1$) the S.O.H. predictions for the onset of the loss of ellipticity are well into the fiber contact zone of the composite and hence are not shown here.

4.4. *Onset-of-failure curves for isochoric loading paths*

Next, in Figs. 5–14, we investigate the influence of microgeometry, initial fiber volume fraction, fiber section aspect ratio, matrix constitutive law and fiber-matrix interface strength for the isochoric loading paths described in (3.3) and (3.4).

In Fig. 5 are presented the onset-of-failure curves for composite elastomers with a perfectly periodic hexagonal arrangement of circular section fibers (r=1), an initial fiber volume fraction of $f_0=\pi/16\approx 0.2$ and a neo-Hookean matrix ($\kappa/\mu=10$). More specifically, in Fig. 5a are plotted, in strain space (ε_1 vs γ_{21} and γ_{12}), the curves for the macroscopic

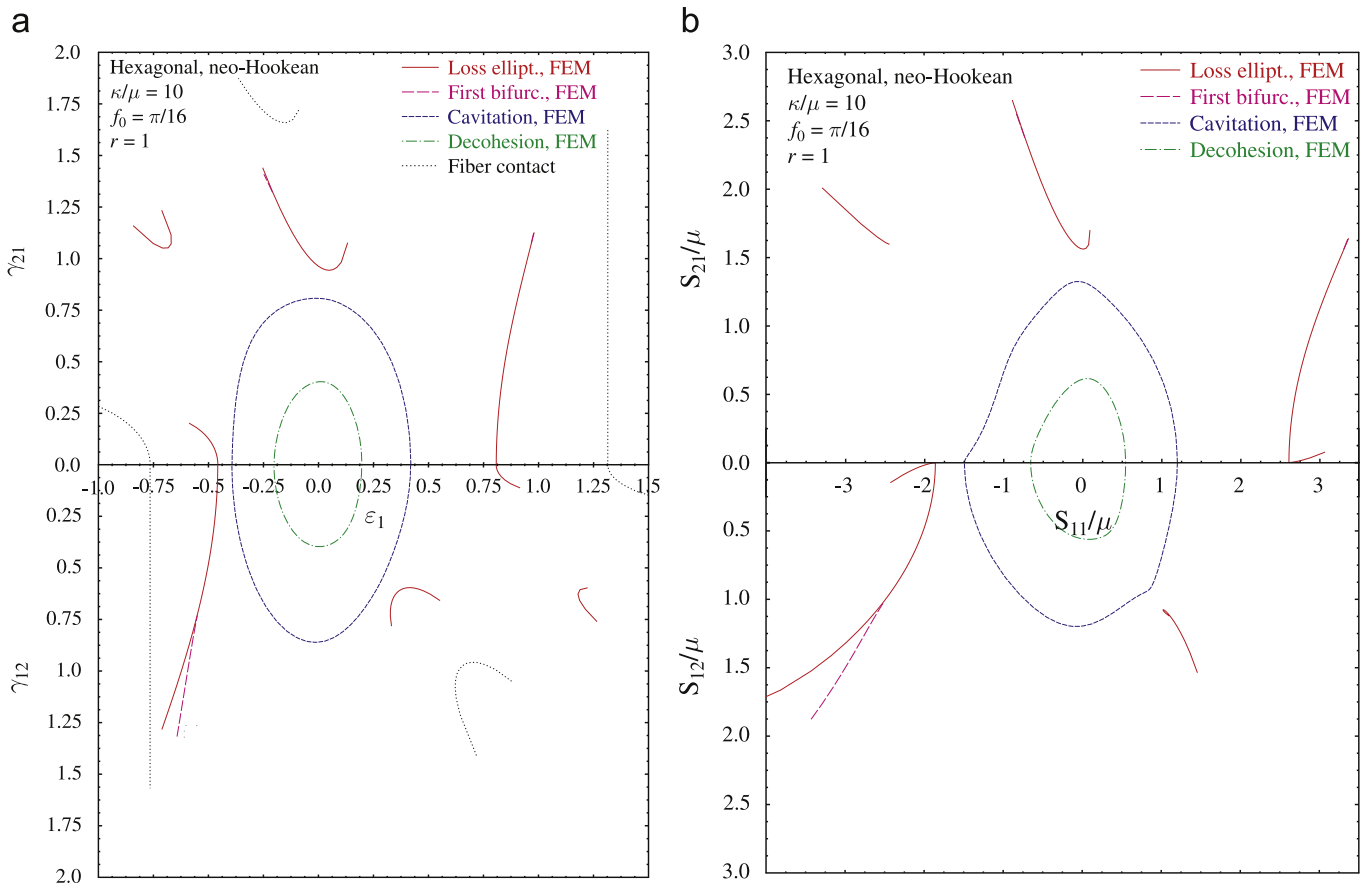

Fig. 5. Onset-of-failure curves for hexagonal microgeometry, neo-Hookean matrix ($\kappa/\mu = 10$) composite of initial fiber volume fraction ($f_0 = \pi/16 \approx 0.2$) with circular section fibers (r=1), which is subjected to isochoric plane-strain loading: (a) results in macroscopic strain space and (b) in dimensionless macroscopic stress space. Macroscopic loss of ellipticity is depicted by solid lines, onset of first bifurcation by big dash lines, matrix cavitation by small dash lines, fiber decohesion by dot–dash lines and fiber contact by dotted lines. Results are based on F.E.M. calculations.

onset-of-failure (loss of ellipticity of the homogenized moduli, in continuum lines), the microscopic onset-of-failure (first bifurcation, in big dash lines), the onset-of-cavitation in the matrix (small dash lines) and the onset-of-decohesion at the fiber-matrix interface (dot–dash lines). The locus of strains corresponding to fiber contact are also marked (dotted lines). The same results, plotted in dimensionless stress space — corresponding nominal stresses over shear modulus (S_{ij}/μ) — are presented in Fig. 5b. The results reported in Fig. 5 are based on F.E.M. calculations.

Unlike the results in the previous subsection, for isochoric strain paths, there is a well ordered sequence of instabilities for this initially isotropic, periodic composite. Along any given radial loading path, a fiber-matrix decohesion always occurs first followed by matrix cavitation at about twice the strains of decohesion. Consequently the corresponding onset-of-failure curves are closed, non-intersecting, simple curves about the origin. Onset of first bifurcation always occurs after the onset of matrix cavitation, but not for all radial loading paths, as there are significant fan-shaped zones about the origin in which no bifurcation instability occurs, i.e., the unit-cell-periodic solution is always stable. For the isochoric biaxial stretching loading paths ($\varphi = 0, \pi$), the first bifurcation always coincides with a loss of ellipticity, i.e., the critical mode has a wavelength much larger than the unit cell dimensions. For loading paths with other orientations, a first bifurcation might occur at a finite wavelength. Local critical modes, i.e., modes involving several unit cells in each direction, are found for approximately $\varphi \in [48^\circ, 50^\circ] \cup [98^\circ, 100^\circ]$ for γ_{21} loading and $\varphi \in [116^\circ, 127^\circ]$ for γ_{12} loading.

The fact that a decohesion instability always occurs prior to a matrix cavitation is also reflected in the stress plot of Fig. 5b, where the corresponding onset-of-failure curves are closed, non-intersecting, simple curves about the origin, although they look more distorted than their almost elliptical counterparts in strain space. At any rate, the general conclusion for the hexagonal microgeometry, periodic composite with circular section fibers and a neo-Hookean matrix — when ignoring the fiber-matrix interface strength — is that it will always fail by matrix cavitation when subjected to a volume-preserving macroscopic loading path. A microscopic bifurcation or a macroscopic loss of ellipticity instability is possible at larger strains for some loading paths, always before reaching fiber contact. The fact that a decohesion is found here to occur prior to cavitation is a result of our interface strength choice and it is possible, as it will be seen later, that decohesion can occur after cavitation for composites with stronger interfaces.

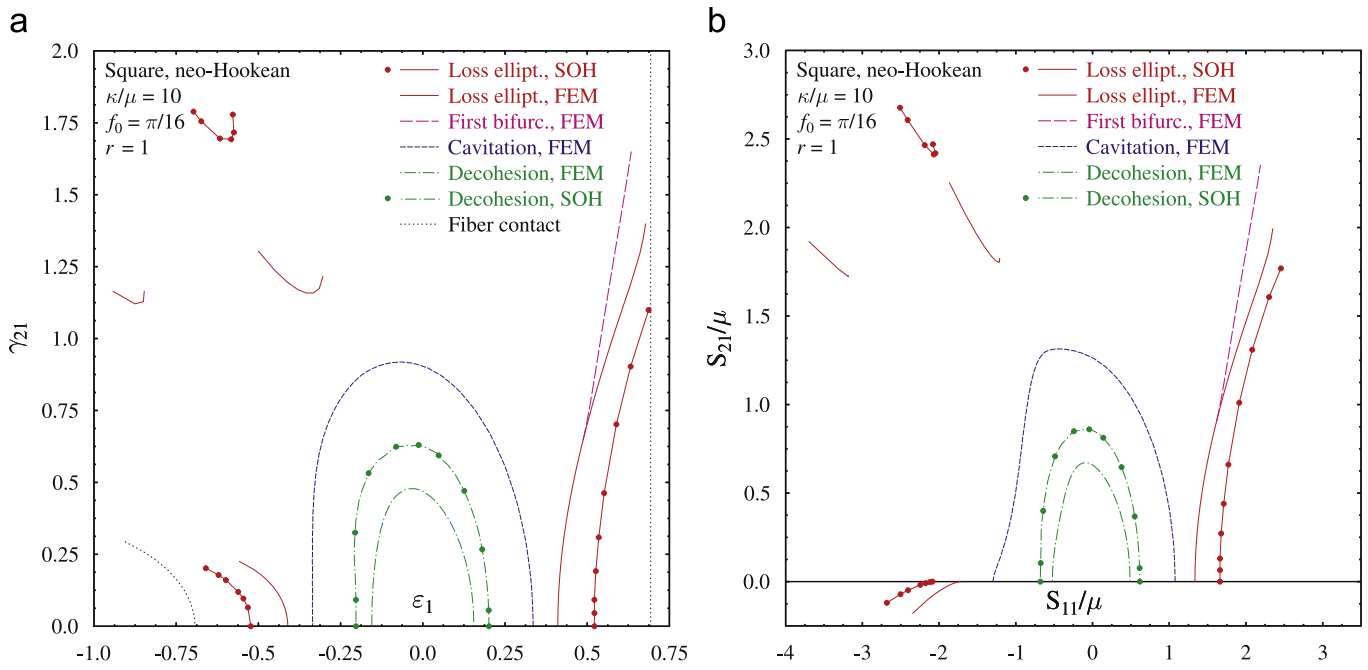

Fig. 6. Onset-of-failure curves for square microgeometry, neo-Hookean matrix ($\kappa/\mu=10$) composite of initial fiber volume fraction ($f_0=\pi/16\approx 0.2$) with circular section fibers (r=1), which is subjected to isochoric plane-strain loading: (a) results in macroscopic strain space and (b) in dimensionless macroscopic stress space. Macroscopic loss of ellipticity is depicted by solid lines, onset of first bifurcation by big dash lines, matrix cavitation by small dash lines, fiber decohesion by dot–dash lines and fiber contact by dotted lines. Results based on F.E.M. calculations are shown in solid lines while results based on S.O.H. calculations are shown in bullet-marked lines.

The results presented in Fig. 6 correspond to a periodic composite with the same matrix material, circular section fibers and initial fiber volume fraction as in Fig. 5, but with a square (instead of hexagonal) microgeometry. The same line drawing convention as in Fig. 5a is used here for plotting the different onset-of-failure curves. Moreover, and in addition to the F.E.M. results (solid lines), results from S.O.H. calculations for the same composites are also presented (bullet-marked lines). Due to the symmetry of the square microgeometry only γ_{21} loading needs to be considered for this case; had γ_{12} calculations been carried out and the corresponding graphs plotted as in Fig. 5, the curves would have been point-symmetric with respect to the origin.

The conclusions are fairly similar to the ones obtained for the hexagonal microgeometry, i.e., that along any radial loading path a decohesion always precedes (at about half the strain) a matrix cavitation instability. A loss of macroscopic ellipticity follows for paths ($\varphi=0,\pi$), but not for simple shearing ($\varphi=\pi/2$). Also there is a larger, than for the hexagonal microgeometry, range of loading paths where a first bifurcation precedes the loss of macroscopic ellipticity, found for approximately $\varphi\in[53^\circ,69^\circ]$. Also notice that due to the symmetry of the composite, all corresponding critical points are symmetric along the ε_1 axis.

It is worth noticing that the S.O.H. approximation does a fairly good job in predicting the decohesion and loss of ellipticity strains and stresses, considering the significant initial fiber volume fraction ($f_0=\pi/16\approx 0.2$) of the composite. The shapes of the S.O.H. curves are similar to the corresponding F.E.M. ones, with the S.O.H. approximation consistently overpredicting the stresses and strains at the onset-of-failure. Also notice that, like the F.E.M. method, the S.O.H. approximation predicts decohesion inside the cavitation-safe region in both strain (see Fig. 6a) and stress (see Fig. 6b) space. Similarly the loss of ellipticity is predicted by the S.O.H. to occur prior to fiber contact for most radial paths; however, for paths with $\varphi\in[58^\circ,90^\circ]$ the S.O.H. method predicts a macroscopic loss of ellipticity past fiber contact and the corresponding part of the failure curve is not shown, for it is physically meaningless.

The influence of the initial fiber volume fraction on the onset-of-failure in periodic composites is considered next in Fig. 7, where the results correspond to a square microgeometry composite, with the same neo-Hookean matrix material and initial circular section fibers as the composite in Fig. 6, but with two different initial fiber volume fractions; f_0=0.1 in (a) and f_0=0.3 in (b). The same line drawing convention as in Fig. 6a is also used here for plotting the different onset-of-failure curves.

In comparing Fig. 7a and b and also Fig. 6a, one observes the following trends: increasing of the initial fiber volume fraction decreases all critical strains (i.e., for first bifurcation, loss of ellipticity, decohesion and cavitation) resulting in a (rather approximately) self-similar shrinking of the corresponding curves about the origin. This behavior is expected from the resulting higher strain/stress concentrations between the fibers that result at the higher fiber volume fraction composites loaded at the same levels of macroscopic strain as their smaller fiber volume fraction counterparts. Although the sequence for the onset-of-failure phenomena remains the same (decohesion, followed by cavitation, a bifurcation or a

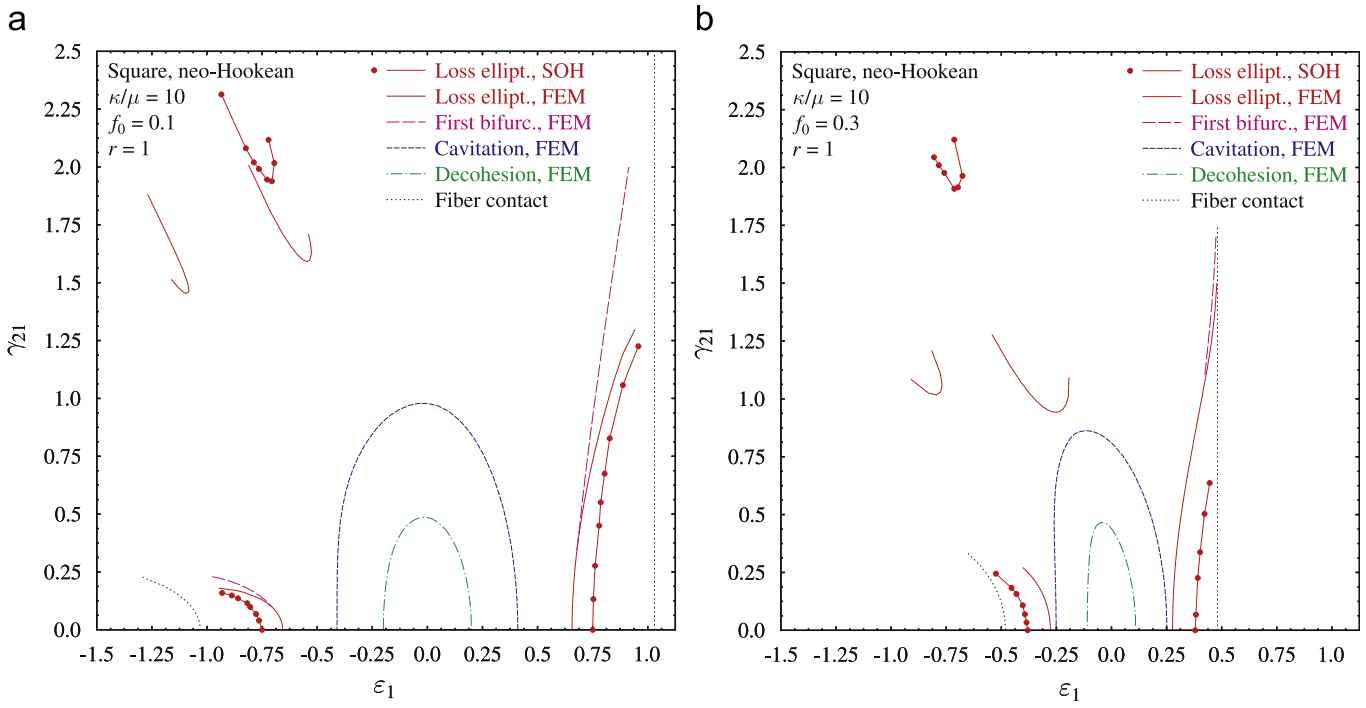

Fig. 7. Onset-of-failure curves for square microgeometry, neo-Hookean matrix ($\kappa/\mu = 10$) composites of different initial fiber volume fractions: (a) f_0=0.1 and (b) f_0=0.3. In both cases, the fibers have circular sections (r=1) and are subjected to isochoric plane-strain loading. Macroscopic loss of ellipticity is depicted by solid lines, onset of first bifurcation by big dash lines, matrix cavitation by a small dash lines, fiber decohesion by dot–dash lines and fiber contact by dotted lines. Results based on F.E.M. calculations are shown in solid lines while results based on S.O.H. calculations are shown in bullet-marked lines.

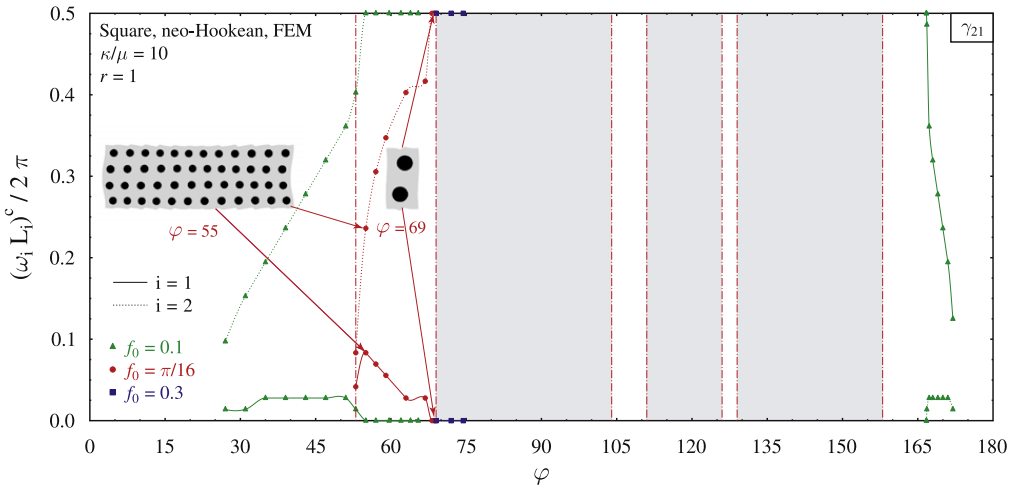

Fig. 8. Dimensionless critical wavenumber at the onset of the first bifurcation for square microgeometry, neo-Hookean matrix ($\kappa/\mu = 10$) composites with circular section fibers (r=1), as a function of the load path angle (φ), for three different initial fiber volume fractions ($f_0 = 0.1$, $\pi/16$,0.3). For $f_0 = \pi/16$, we separate by vertical lines the load path angle range according to the nature of the first instability found: finite, infinite wavelength or no instability at all, with the latter shaded in grey. For the same composite, we also show in inserts the fundamental cell of two finite wavelength critical modes.

loss of ellipticity — depending on the critical eigenmode's wavelength), the loss of ellipticity curves are much closer to their cavitation counterparts for the highest value of f_0=0.3, as seen in Fig. 7b.

The study of the eigenmodes merits special attention and is presented next. In Fig. 8 is plotted the dimensionless critical wavenumber $(\omega_i L_i)^c/2\pi$ as a function of the load path angle φ, for the square microgeometry, neo-Hookean matrix ($\kappa/\mu = 10$) composites with circular section fibers ($r = 1$) studied in Figs. 6 and 7. The dimensionless critical wavenumber along the X_1 direction, $(\omega_1 L_1)^c/2\pi$, is plotted in solid lines, while its counterpart along the X_2 direction, $(\omega_2 L_2)^c/2\pi$, is plotted by dotted lines. Results corresponding to initial fiber volume fractions $f_0 = 0.1, \pi/16, 0.3$ are shown, respectively, in triangle-marked, circle-marked and square-marked lines. For $f_0 = \pi/16 \approx 0.2$, we separate by vertical lines the load path angle range according to the nature of the first instability found: finite, infinite wavelength or no instability at all, with the

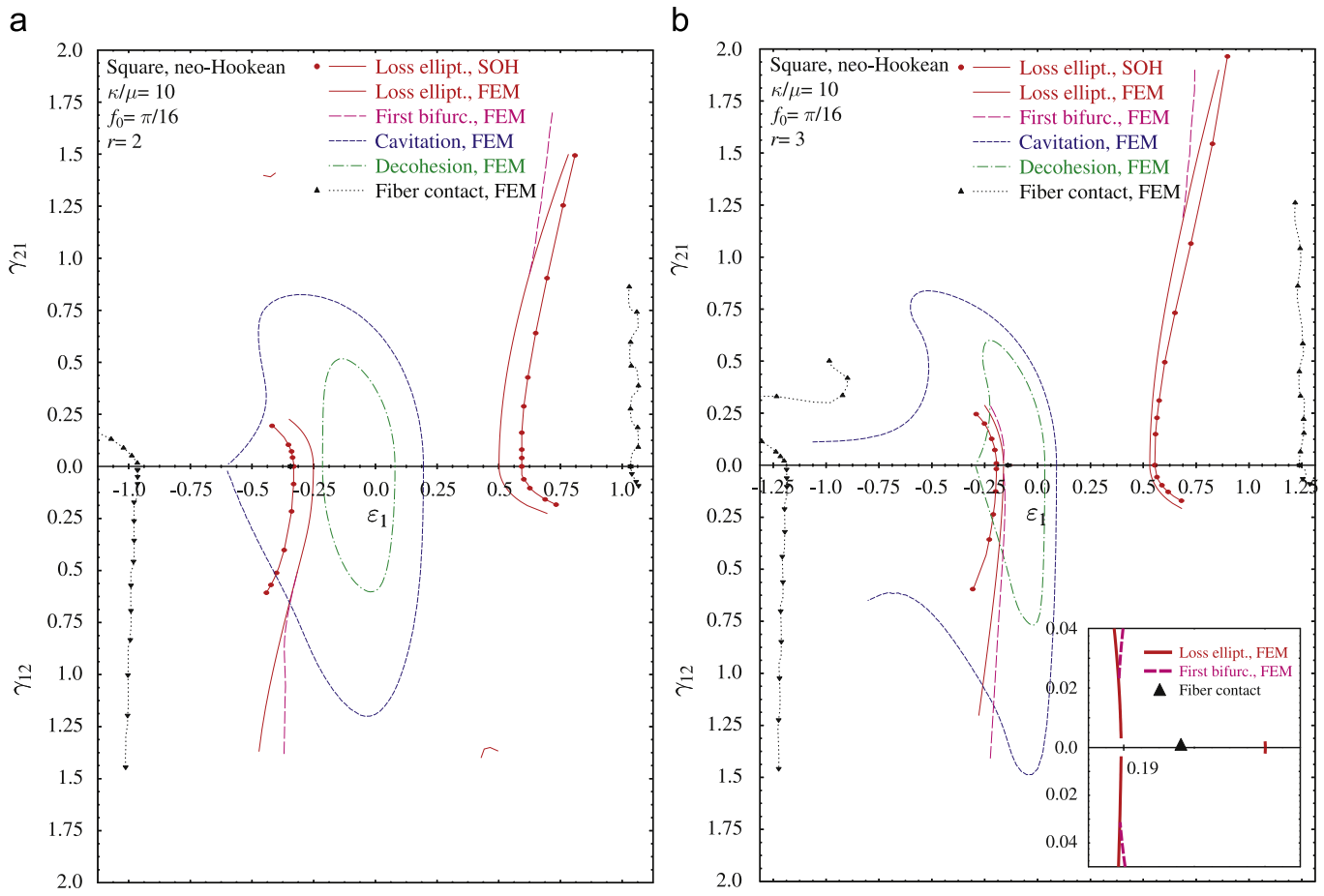

Fig. 9. Onset-of-failure curves for square microgeometry, neo-Hookean matrix ($\kappa/\mu=10$) composites of initial fiber volume fraction ($f_0=\pi/16\approx 0.2$) with elliptical section ($r>1$) fibers which are subjected to isochoric plane-strain loading. Results in macroscopic strain space are shown for (a) elliptical section fibers with aspect ratio r=2 and (b) elliptical section fibers with aspect ratio r=3. Macroscopic loss of ellipticity is depicted by solid lines, onset of first bifurcation by big dash lines, matrix cavitation by small dash lines, fiber decohesion by dot–dash lines and fiber contact by triangle-marked dotted lines. Also presented by insert in (b) is a zoom of the singularity in the loss of macroscopic ellipticity for loading along a load path angle $\varphi=\pi$. Results based on F.E.M. calculations are shown in solid lines while results based on S.O.H. calculations are shown in bullet-marked lines.

latter shaded in grey. For the same composite, we also show in an insert the fundamental cell of two finite wavelength critical modes, i.e., for $\varphi=55^\circ$ and 69°. The arrows in each mode point to the corresponding critical wavelengths in each direction. All results are based on F.E.M. calculations.

The most significant feature in Fig. 8 is that the range of loading angles for which a local mode is found (i.e., when the first bifurcation instability has a finite wavelength), increases as the fiber volume fraction decreases. Thus, while for the highest fiber volume fraction, f_0=0.3, finite wavelength critical modes are possible only for a narrow interval near $\varphi=70^\circ$, for the lowest volume fraction examined, f_0=0.1, finite wavelength critical modes are found for a much wider range of φ and in two different intervals, the larger for $\varphi<\pi/2$ and the smaller for $\varphi>\pi/2$. Another interesting feature is the remarkable "*richness*" of the eigenmodes, as evidenced by the fact that for the two smaller fiber volume fractions, the dimensionless critical wavenumber can reach a wide range of values between 0 and 0.5, which means that the fundamental cell of the critical mode can be large indeed (e.g., see insert for the critical mode for $\varphi=55^\circ$). This result is in contrast with the corresponding result for the porous elastomers (see Michel et al., 2007; Bertoldi et al., 2008), where the local modes found for circular section holes invariably corresponded to $(\omega_i L_i)^c/2\pi=0.5$, i.e., the fundamental cell for the critical modes involved at most 2×2 cells.

All calculations thus far pertain to composites with circular fiber sections (r=1). However, it has recently been found by Lopez-Pamies and Ponte Castañeda (2006b) that the presence of aligned fibers with elliptical cross-section can destabilize composites, especially for compressive loading aligned with the fiber section's major axis. This destabilization, detected in Lopez-Pamies and Ponte Castañeda (2006b) by a loss of ellipticity of the composite's homogenized moduli, is highly sensitive to the fiber section's aspect ratio and is due to a rotation of the fibers about their axes (i.e., about X_3) that alleviates stress concentrations. It is therefore imperative to investigate the influence of the fiber section's aspect ratio r on the composite's onset-of-failure curves, which is the subject of Fig. 9.

The results presented in Fig. 9 correspond to a periodic composite with the same square microgeometry, matrix material and initial fiber volume fraction as in Fig. 6, but with non-circular fiber cross-sections ($r>1$). More specifically the

results in Fig. 9a correspond to elliptical section fibers with aspect ratio $r=2$, while Fig. 9b pertains to calculations with $r=3$. The same line drawing convention as in Fig. 6 is also used here for plotting the different onset-of-failure curves. Due to the elliptical section fibers, the symmetry arguments used for the calculations in Fig. 6 no longer hold. Consequently both γ_{21} and γ_{12} loadings are considered and Fig. 9 is plotted similarly to Fig. 5.

The decohesion and cavitation curves are still closed simple curves (i.e., an interface decohesion is followed by a matrix cavitation along any radial loading path direction) in Fig. 9a, but are shifted along the compression direction of the ε_1 axis. For tension along the major axis of the fiber's section ($\varepsilon_1>0$), the loss of ellipticity occurs well after matrix cavitation (at more than twice the strain of cavitation). In contrast, for compression along the major axis of the fiber's section ($\varepsilon_1<0$), the loss of ellipticity appears at slightly higher strains than decohesion and well below the strain required for the matrix to cavitate (which now occurs at about twice the strain for the loss of ellipticity). Moreover, the loss of ellipticity for compression along the major axis of the fiber's section occurs at about -0.25 while for tension is found at about $+0.5$. This tension/compression asymmetry can be easily understood from the fact that compressing the elliptical fiber along the major axis of its section is an unstable deformation mode, since a slight rotation in either direction can alleviate the stress concentration occurring at the shortest distance between fibers. As a result of this destabilization mechanism for the elliptical fiber composite, for strains $\varepsilon_1<0$, a large part for the loss of ellipticity curve lies inside the cavitation-free region — in contrast to the circular section fiber composite of Fig. 6a.

Also notice that the loss of ellipticity is occurring for a narrow range of loading paths near $\varphi\approx 110^\circ$ for the γ_{21} case and $\varphi\approx 70^\circ$ for the γ_{12} case. The S.O.H. method misses these two small isolated branches but captures rather well the two loss of ellipticity branches that intersect the ε_1 axis. It should also be mentioned at this point that unlike the circular section fiber cases, no simple geometric calculation can determine the locus of fiber contact in strain space for paths off the ε_1 axis, since the rotation of the fibers is non-zero and is dictated by equilibrium. For these paths, as explained in Appendix A, a numerical method is used, thus explaining the slightly wavy nature of the corresponding curves (triangle-marked dotted lines) appearing in Fig. 9.

Increasing the fiber section's aspect ratio to $r=3$ further distorts the decohesion and cavitation curves (the latter is no longer closed) and shifts the loss of ellipticity branch in the $\varepsilon_1<0$ zone closer to the origin, as seen in Fig. 9b. Indeed, by increasing the aspect ratio, one further destabilizes the $\varepsilon_1<0$ path and a loss of ellipticity is now found at about $\varepsilon_1=-0.12$, prior to fiber contact, which for this path occurs at about $\varepsilon_1=-0.14$. It is remarkable that addition of a slight amount of shear ($\varphi=179^\circ$), induces a rotation of the fiber about its axis and delays considerably the loss of ellipticity, which occurs at about $\varepsilon_1=-0.19$, thus explaining the discontinuity of the loss of ellipticity curve near its intersection with the $\varepsilon_1<0$ semi-axis, as seen from the insert in Fig. 9b. In contrast to the previous cases studied, for the $\varepsilon_1<0$ loadings, the loss of ellipticity is the first instability encountered in the loading process, prior to decohesion and well before cavitation; the latter instability is not even found for a large range of loading paths, as seen from the open form of the cavitation curve in Fig. 9b. Finally, it should also be pointed out here that the increase of the aspect ratio results in the substantial improvement of the loss of ellipticity predictions by the S.O.H. method, as one can see by comparing Fig. 9a and b.

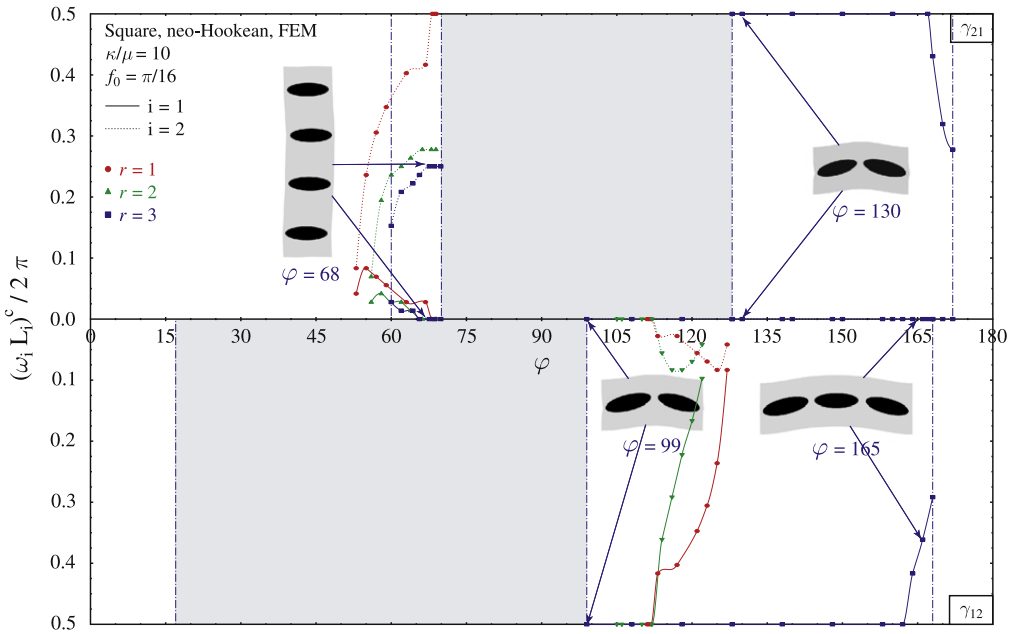

Fig. 10. Dimensionless critical wavenumber at the onset of the first bifurcation for square microgeometry, neo-Hookean matrix ($\kappa/\mu=10$) composites with fiber sections of three different aspect ratios (r=1,2, 3), as a function of the load path angle (φ), for an initial fiber volume fraction ($f_0=\pi/16\approx 0.2$). For r=3, we separate by vertical lines the load path angle range according to the nature of the first instability found: finite, infinite wavelength or no instability at all, with the latter shaded in grey. For the same composite, we are also showing in insert the fundamental cell of several finite wavelength critical modes.

The study of the eigenmodes for the elliptical inclusion composites of Fig. 9 is particularly interesting. In Fig. 10, the dimensionless critical wavenumber $(\omega_i L_i)^c/2\pi$ is plotted as a function of the load path angle φ, for the square microgeometry, neo-Hookean matrix ($\kappa/\mu=10$) composites with initial fiber volume fraction $f_0=\pi/16\approx 0.2$. The dimensionless critical wavenumber along the X_1 direction, $(\omega_1 L_1)^c/2\pi$, is plotted in solid lines, while its counterpart along the X_2 direction, $(\omega_2 L_2)^c/2\pi$, is plotted by dotted lines. Results corresponding to elliptical fiber section aspect ratios $r=1, 2, 3$ are shown, respectively, in circle-marked, triangle-marked and square-marked lines (the circular section fiber results are included for comparison). For $r=3$, we separate by vertical lines the load path angle range according to the nature of the first instability found: finite, infinite wavelength or no instability at all, with the latter shaded in grey. For the same composite, we also show in an insert the fundamental cell of four finite wavelength critical modes, i.e., for $\varphi=68^\circ$ and 130° for γ_{21} loading and $\varphi=99^\circ$ and 165° for γ_{12} loading. The arrows in each fundamental cell point to the corresponding critical wavelengths in each direction. All results are based on F.E.M. calculations.

For radial paths with angles φ away from 0 or π, a finite wavelength bifurcation is found to precede the loss of macroscopic ellipticity for all aspect ratios, as seen in Fig. 10. Notice the considerable increase, compared to $r=1, 2$, of the load path angle range for which a local mode is found for $r=3$. More specifically, for γ_{21} loading a local bifurcation instability is found for $60^\circ<\varphi<70^\circ$ and for $128^\circ<\varphi<172^\circ$, while for γ_{12} loading a local bifurcation instability is found for $99^\circ<\varphi<168^\circ$. In a large part of these load path intervals, the critical eigenmode is anti-periodic mode along X_1 and periodic along X_2 as seen in Fig. 10. Also the small dimensionless wavenumbers found for some load path angles, indicate critical modes involving large numbers of unit cells, particularly along the X_1 direction as seen from the low value of $(\omega_1 L_1)^c/2\pi$ in the interval $\varphi\in[60^\circ,70^\circ]$ for γ_{21} loading and $r=3$.

For completeness, one must also look at the fiber rotation — for the principal (unit-cell-periodic) solution branch — as a function of the load parameter (λ), defined in (3.4), for different loading paths (φ). The results for the square microgeometry, neo-Hookean matrix ($\kappa/\mu=10$) composite with initial fiber volume fraction ($f_0=\pi/16\approx 0.2$), based on F.E.M. (solid lines) and S.O.H. (bullet-marked lines) are given in Fig. 11. For the circular section ($r=1$) fiber case, seen in Fig. 11a, there is a remarkable agreement between the F.E.M. and S.O.H. results for all loading paths for $\lambda<0.25$, while for the simple shear case $\varphi=\pi/2$ the agreement between the two methods extends all the way for $\lambda=1.0$.

For the elliptical fiber section ($r=2$) case seen in Fig. 11b, the S.O.H. approximation does a rather inaccurate job, even for small values of the load parameter λ. It is worth pointing out in Fig. 11 that fiber rotation is not necessarily a monotonically increasing function of the applied load parameter, as one might naively expect. Notice for example that for γ_{21} loading on a path with $\varphi=30^\circ$, the rotation is initially in the counterclockwise direction, as expected from the γ_{21} shearing. This rotation eventually reverses its direction due of course to the isochoric biaxial stretching ($\varepsilon_2=-\varepsilon_1$) component of the loading along the principal axes of the composite, which constitutes a shearing at 45° that tends to rotate the fibers in the clockwise direction (similar results for random systems were discussed in Section 4.5 of Lopez-Pamies and Ponte

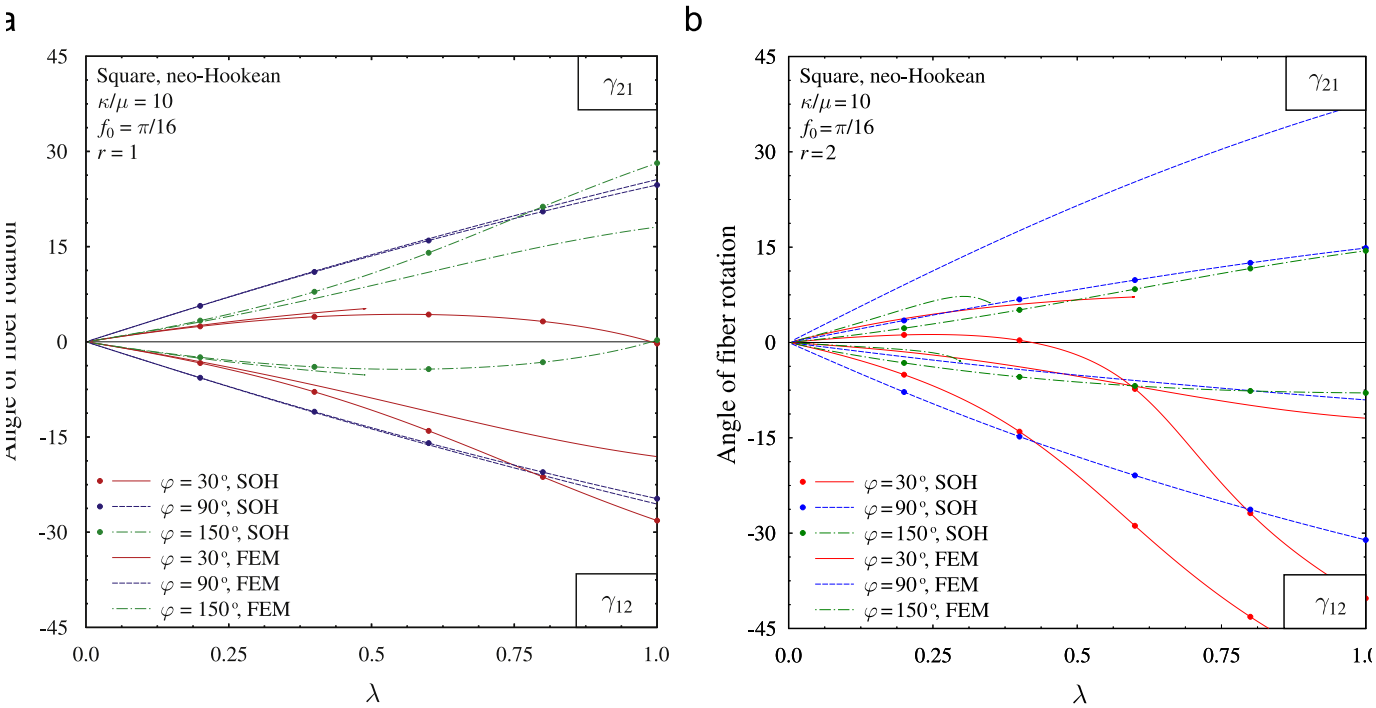

Fig. 11. Fiber rotation as a function of the applied stretch ratio (λ) at different load path angles (φ) for square microgeometry, neo-Hookean matrix ($\kappa/\mu=10$) composite with initial fiber volume fraction ($f_0=\pi/16\approx 0.2$) of (a) circular section fibers ($r=1$) and (b) elliptical section fibers ($r=2$), which is subjected to isochoric plane-strain loading. Results based on F.E.M. calculations are shown in solid lines while results based on S.O.H. calculations are shown in bullet-marked lines.

Castañeda, 2006b). This isochoric biaxial stretching loading component eventually dominates and the sign of the rotation changes. The effect is more dramatic for the elliptical inclusion as seen by comparing the fiber rotations for the γ_{21} loading on a path with $\varphi = 30^{\circ}$ between Fig. 11a and b.

The reason for the inaccuracy in the rotations predicted by the S.O.H. method for the elliptical section fibers is partly that the interaction effects are very strong for elliptical inclusions at a volume fraction of $f_0 \approx 0.20$, and the Hashin–Shtrickman-type approximation cannot capture them accurately. Unpublished calculations at much lower concentrations by Michel and Ponte Castañeda (2009) do show a much better agreement between the rotations predicted by the F.E.M. and the S.O.H. methods.

In Fig. 12a, a more detailed investigation of the influence of microgeometry, ranging from perfectly periodic to random, is presented for various fiber section aspect ratios (r) and fiber volume fractions (f_0). In particular, Fig. 12a depicts the loss of ellipticity curves for square periodic — perfect and imperfect, as explained below — and random microgeometries, neo-Hookean matrix ($\kappa/\mu = 10$) composites with an initial fiber volume fraction f_0=0.1 and different fiber section aspect ratios (r). On the other hand, Fig. 12b shows results for composites with the same microgeometries and matrix material as in Fig. 12a, a fiber section aspect ratio r=3 and different initial fiber volume fractions (f_0). Results for the square microgeometries are based on F.E.M. calculations (solid lines for perfect microgeometry, hollow square-marked lines for imperfect 3×3 aggregates) and for random, isotropic, polydisperse microgeometries on S.O.H. calculations (bullet-marked lines). For the square microgeometry with f_0=0.1 and r=3, the macroscopic loss of ellipticity is depicted by solid line. The loss of ellipticity for the random microgeometry composite with f_0= 0.1 and r=5 in (a) is depicted by a dotted line. The random microgeometry composites with $f_0 = \pi/16$,0.3 and r= 3 in (b) are depicted by dashed and dotted lines, respectively. For the case of loading along $\varphi = 0,\pi$, the loss of ellipticity strain (ε_1) as a function of the fiber section aspect ratio (r) and as a function of the initial fiber ratio (f_0) are presented by inserts in Fig. 12a and b, respectively.

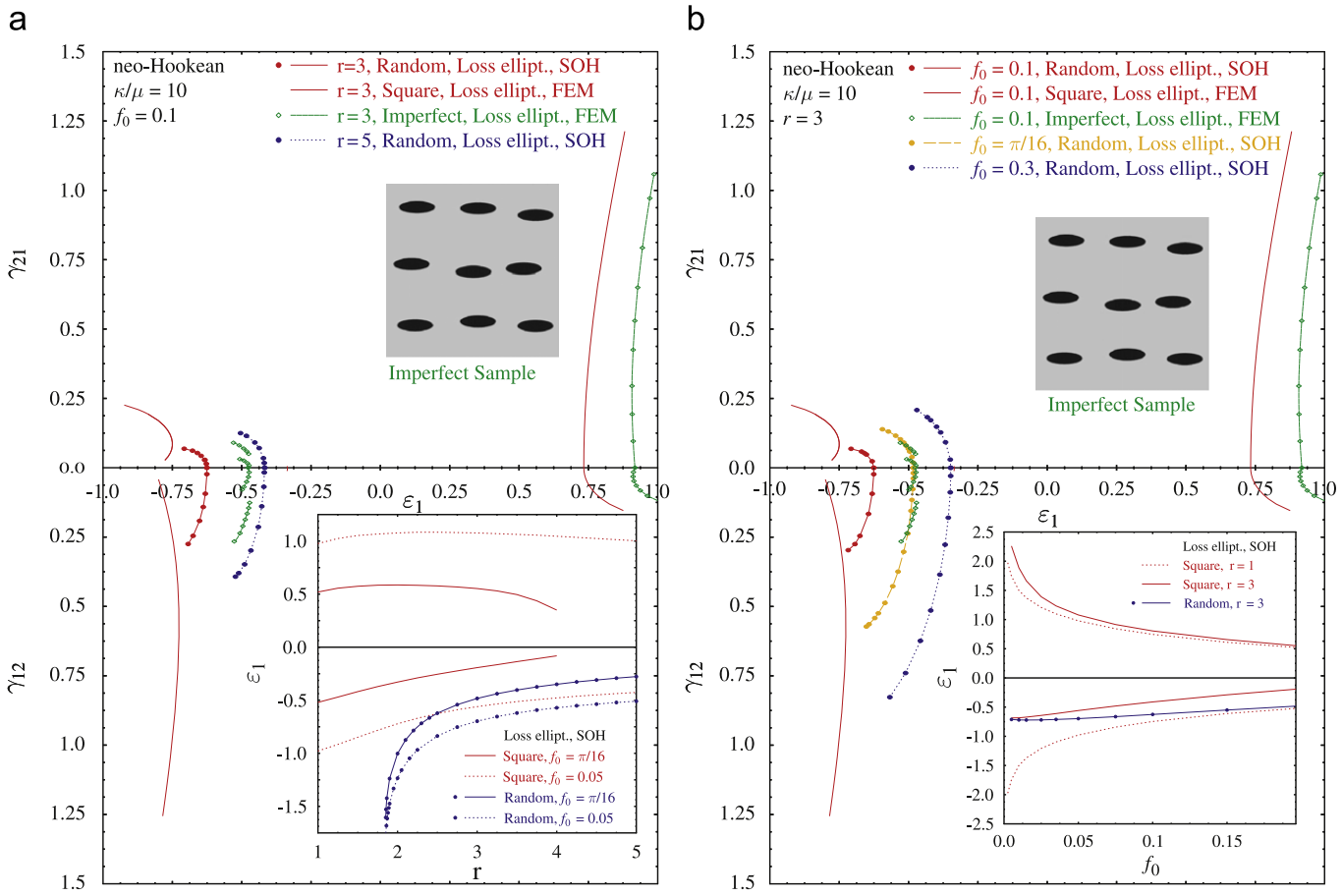

Fig. 12. Influence of (a) fiber section aspect ratio (r) and (b) initial fiber volume fraction (f_0), on the loss of ellipticity curves for square and random microgeometry, neo-Hookean matrix ($\kappa/\mu = 10$) composites, which are subjected to isochoric plane-strain loading. For the base case (f_0=0.1 and r=3) the macroscopic loss of ellipticity is depicted by solid lines. The loss of ellipticity for the random microgeometry composite with f_0=0.1 and r=5 in (a) is depicted in dotted lines. The random microgeometry composites with $f_0 = \pi/16$,0.3 and r=3 in (b) are depicted by dashed and dotted lines, respectively. For the loading path along $\varphi = \pi$, the critical strain (ε_1) at the onset of the loss of ellipticity as a function of the fiber section aspect ratio (r) and as a function of the initial fiber ratio (f_0) are presented by inserts in (a) and (b), respectively. Results for square microgeometries — perfect or imperfect — are based on F.E.M. calculations and shown in solid lines for perfect microgeometry and in hollow square-marked lines for imperfect 3×3 aggregates, while for random, isotropic, polydisperse microgeometries are based on S.O.H. calculations and shown in bullet-marked lines.

Starting with Fig. 12a, observe that the loss of ellipticity curve for the perfect square microgeometry composite has a discontinuity at $\varphi=\pi$, as expected from the discussion of Fig. 9b, since a small amount of shearing stabilizes the composite when it is compressed along the major axis of the elliptical fiber's cross-section (the loss of ellipticity for $\varphi=\pi$ occurs at about $\varepsilon_1=0.33$). The loss of ellipticity of the corresponding 3×3 imperfect aggregate, which results by a perturbation of a perfect 3×3 aggregate by randomly moving the centers by a maximum distance 0.125 L_1 about their perfect periodic positions, occurs as expected at higher strains for paths near $\varphi=0$ and π. However, unlike the $\varphi<\pi/2$ loading paths, where the imperfect aggregate always loses ellipticity at higher strains than its perfect counterpart, the imperfect aggregate can lose ellipticity well before its perfect counterpart for paths with $\varphi>\pi/2$. Moreover the loss of ellipticity curve for the imperfect aggregate shows discontinuities with respect to φ for both γ_{21} and γ_{12} loadings, as does its perfectly periodic counterpart. However, unlike the $\varphi<\pi/2$ where the geometry imperfection leads to higher critical strains, for loadings with $\varphi>\pi/2$ away from the $\varphi=\pi$ neighborhood, the loss of ellipticity strains for the imperfect composite are, surprisingly, considerably lower than for the perfect one.

The comparison of the S.O.H. estimate for the random composite with the same matrix material, fiber volume fraction f_0 and fiber aspect ratio r as the periodic composites finds a loss of ellipticity for $\varphi>\pi/2$ but none for $\varphi<\pi/2$. The loss of ellipticity for $\varphi>\pi/2$ shows no singularity near $\varphi=\pi$ and corresponds to strains well above those for the loss of ellipticity of the imperfect aggregate, but surprisingly below those for the corresponding perfect composite along paths away of the $\varphi=\pi$ neighborhood. Increasing the fiber section's aspect ratio further destabilizes the composite, as the results for the random polydisperse composite with to r=5 show in Fig. 12a. In this connection, notice also from the insert that for random polydisperse composites the loss of ellipticity under isochoric biaxial loading ($\varphi=0,\pi$) as a function of r has an asymptote about r=1.8 below which no loss of ellipticity is found for all values of f_0 considered.

Continuing with Fig. 12b, which investigates the loss of ellipticity for the same microgeometry and matrix material composites as in Fig. 12a, but with different f_0 and only for r=3, notice that for the random microgeometry composite, an increase in the fiber volume fraction from f_0=0.1 to 0.3 reduces considerably the loss of ellipticity strains for loading paths with $\varphi>\pi/2$ (no loss of ellipticity is found for loading paths with $\varphi<\pi/2$). Since for paths with $\varphi>\pi/2$, an increase in f_0 implies higher compressive stresses between more closely spaced fibers — for the same macroscopic strain — the corresponding instability occurs at decreasing macroscopic strains, as seen in Fig. 12b. For each f_0, the most unstable loading path occurs when $\varphi=\pi$, while the presence of additional shearing for paths with $\varphi\neq\pi$ rotates the fibers about their axes and lowers compressive stress concentrations, thus leading to higher critical strains as evidenced by the concave shape of the corresponding curves in Fig. 12b.

There is more information linking the loss of ellipticity to fiber volume fraction for periodic and random polydisperse composites in the insert of Fig. 12b, which has been calculated for isochoric biaxial loading ($\varphi=0,\pi$). It is worth noticing that for r=3 and $\varphi=\pi$, the loss of ellipticity for the random and square periodic microgeometries converge to the same value at the dilute concentration limit, i.e., as $f_0\to0$. For the square periodic microgeometry, the loss of ellipticity strain

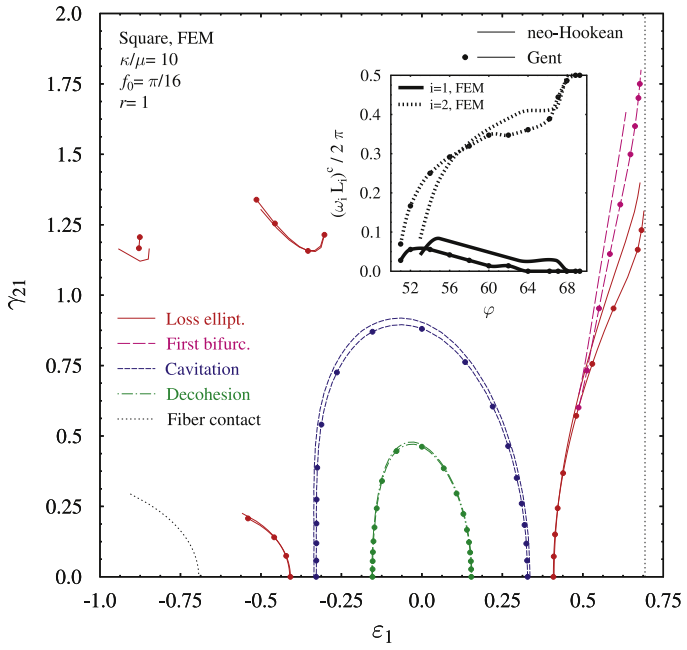

Fig. 13. Influence of matrix constitutive law on the onset-of-failure curves in macroscopic strain space. A neo-Hookean matrix, shown in unmarked lines, and a Gent matrix, shown in bullet-marked lines, periodic composite with square microgeometry are considered both with initial fiber volume fraction ($f_0=\pi/16\approx0.2$) and circular section fibers (r=1), and are subjected to isochoric plane-strain loading. Macroscopic loss of ellipticity is depicted by solid lines, onset of first bifurcation by big dash lines, matrix cavitation by small dash lines, fiber decohesion by dot–dash lines and fiber contact by dotted lines. The dimensionless critical wavenumber at the onset of the first bifurcation as a function of the load path angle is presented by insert (only for values of the load path angle with a finite wavelength critical mode). Results are based on F.E.M. calculations.

increases without bound for $\varphi = 0$ paths (i.e., for $\varepsilon_1 > 0$) as the dilute concentration limit is approached. For the $\varphi = \pi$ paths (i.e., for $\varepsilon_1 < 0$), only the r=3 loss of ellipticity curve converges to a finite value at the dilute concentration limit, for reasons just discussed. The corresponding curve for r=1 for $\varepsilon_1 < 0$ is the same — due to the composite's symmetry — with the curve for $\varepsilon_1 > 0$ and hence the loss of ellipticity strain increases without bound as the dilute concentration limit is approached.

The influence of matrix constitutive law on the onset-of-failure curves for perfectly periodic, square microgeometry composites is shown in Fig. 13. A neo-Hookean matrix (solid lines) and a Gent matrix, (bullet-marked lines) composite are considered both with the same initial fiber volume fraction ($f_0 = \pi/16 \approx 0.2$) and circular section fibers (r=1), which are subjected to plane-strain loading preserving macroscopic incompressibility. All results shown in Fig. 13 are based on F.E.M. calculations. The same line drawing convention as Fig. 5a is used here for plotting the different onset-of-failure curves. The dimensionless critical wavenumber at the onset of the first bifurcation as a function of the load path angle is presented as an insert in Fig. 13.

The choice of matrix material makes practically no difference to the onset-of-decohesion and cavitation in either strain or stress space, as seen in Fig. 13. This observation should come to no surprise in view of the results in Fig. 2 which show that for the same microgeometry, the difference in the macroscopic response between neo-Hookean and Gent matrix composites is negligible for strain levels below $\gamma \approx 1.0$. This observation also explains why the first bifurcation and loss of ellipticity results for the two different composites are close for lower strain levels and start deviating from each other at about the strain levels where their macroscopic response starts being influenced by the matrix material, according to the results in Fig. 2. The difference between the critical wavelengths at the onset of a bifurcation instability seen in the insert of Fig. 13 can also be explained by the fact that an onset of bifurcation instability is the critical one for large enough strains, in the strain range where the matrix material choice starts being important for the composite's macroscopic response. The results in Fig. 13 are a final confirmation of the soundness of the choice, made based on the results of Fig. 2, to do most of the calculations for neo-Hookean matrix composites.

Finally a discussion should be made on the influence of the adopted decohesion criterion which, in all calculations up to this point has been assumed to be $\delta_c \equiv (\sigma_{nn}/\mu)_{max} = 1$. Since, depending on the nature of the fiber-matrix interface, its strength can vary significantly, the decohesion curves for the base case composite (neo-Hookean matrix ($\kappa/\mu = 10$) with initial fiber volume fraction ($f_0 = \pi/16 \approx 0.2$) and circular section fibers (r=1)), have been calculated by F.E.M. in Fig. 14 for four different values of δ_c: for $\delta_c = 1$ (solid lines), for $\delta_c = 2$ (bullet-marked lines), for $\delta_c = 3$ (triangle-marked lines) and for $\delta_c = 4$ (square-marked lines). For comparison, all other type onset-of-failure curves have been included in Fig. 14 using the same line drawing convention employed in this subsection (see corresponding description in Fig. 5).

Notice that by increasing the interface strength, the macroscopic strains at the onset-of-decohesion also increase so that the corresponding curves are approximately self-similar (homothetic) expansions of the $\delta_c = 1$ curve about the origin, as expected from the monotonicity of the material's constitutive response. So, depending on the magnitude of the interface's

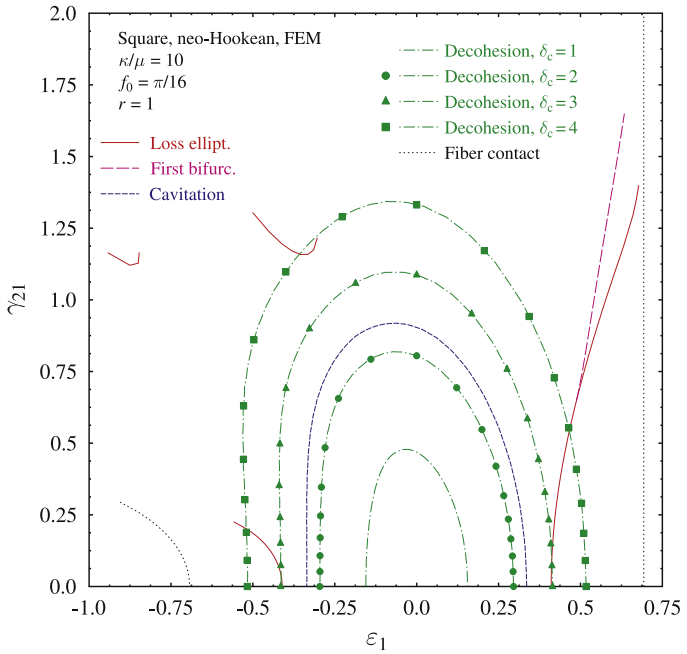

Fig. 14. Influence of decohesion criterion ($\delta_c \equiv (\sigma_{nn}/\mu)_{max}$), depicted by dot–dash lines, for square microgeometry, neo-Hookean matrix ($\kappa/\mu = 10$) composites of initial fiber volume fraction ($f_0 = \pi/16 \approx 0.2$) with circular section fibers (r=1), which are subjected to isochoric plane-strain loading. Solid lines correspond to $\delta_c = 1$, bullet-marked lines to $\delta_c = 2$, triangle-marked lines to $\delta_c = 3$ and square-marked lines to $\delta_c = 4$. For comparison purpose are also shown the macroscopic loss of ellipticity in solid lines, the onset of first bifurcation in big dash lines, the matrix cavitation in small dash lines and fiber contact in dotted lines. Results are based on F.E.M. calculations.

strength, decohesion can occur always prior to cavitation for $\delta_c \leq 2$, after cavitation but before first bifurcation and loss of ellipticity for $\delta_c = 3$ or past the loss of ellipticity for most loading path angles φ for the case of the strongest interface $\delta_c = 4$. Since the strength of the interface can vary considerably (depends on the surface treatment of the fibers), failure by cavitation remains the critical failure mechanism for this composite, independently of the loading path, for adequately strong fiber/matrix interface composites.

The above discussion gives a comprehensive picture of the influence of calculation method, microgeometry (fiber volume fraction, cross-section and distribution), matrix constitutive law and macroscopic load orientation on the microscopic and macroscopic onset-of-failure in hyperelastic fiber-reinforced elastomers under plane-strain loading conditions (perpendicular to the fiber axis direction). A synthesis of these results is the object of the discussion presented in the next section.

5. Discussion and conclusions

The above work is a complement to a previous and analogous investigation by the same authors on porous elastomers (Michel et al., 2007), and provides a detailed study of the connections between microstructural instabilities and their macroscopic manifestations — as captured through their effective properties — in finitely strained fiber-reinforced elastomers, subjected to finite, plane-strain deformations normal to the fiber direction. The work uses the powerful second-order homogenization (S.O.H.) technique, initially developed for random media, to study the onset of failure in fiber-reinforced elastomers with various initial fiber volume fractions, fiber distributions and cross-sections. Perfect and imperfect periodic as well as random fiber distributions are investigated. For the periodic microgeometries these approximate results are compared to more accurate finite element method (F.E.M.) calculations.

Two different types of loading were investigated: biaxial, along the axes of orthotropy of the composite, and isochoric, which preserves the macroscopic incompressibility of the slightly compressible composites investigated here. For the biaxial loading case, only perfectly periodic composites with circular section fibers are considered. The macroscopic onset-of-failure curves in strain space are similar to the ones calculated by Nestorović and Triantafyllidis (2004) for the same matrix material, for square and for diagonal (instead of the present hexagonal) fiber distribution and for slightly different values of the material constants. It is found that for loading paths corresponding to macroscopic contraction, the macroscopic and microscopic onset-of-failure curves, although highly sensitive to the fiber volume fraction and distribution, but considerably less to matrix compressibility, are always coincident. In contrast, for loading paths corresponding to macroscopic dilation, failure is essentially set by matrix cavitation and is insensitive to either fiber volume fraction or fiber distribution. Approximate calculations for the square microgeometry composites based on the S.O.H. method always overpredict the strains at the onset of matrix cavitation and the loss of macroscopic ellipticity. However they capture the shape of the corresponding curves rather faithfully, even for relatively large fiber volume fractions, while their predictions get closer to the corresponding F.E.M. results as the fiber volume fraction decreases.

For loading paths preserving macroscopic incompressibility, the composite's stability behavior is even more complicated. For composites with periodic microgeometries and circular fibers, macroscopic instabilities are found in sectors about $\varphi = 0$ and $\varphi = \pi$ (recall that $\varphi = 0$ corresponds to isochoric biaxial loading with tension along the X_1 axis, while $\varphi = \pi$ corresponds to isochoric biaxial loading with compression along the same axis). However, microscopic instabilities take place before the macroscopic ones for a limited range of loadings along paths with a significant shear component. The distance between these microscopic and macroscopic onset-of-failure curves increases with an increasing amount of shear. For all the fiber volume fractions investigated ($f_0 \leq 0.3$), the microscopic and macroscopic onset-of-failure curves lie always outside the cavitation curve, although these curves approach each other with increasing fiber volume fraction. The critical modes at the onset of bifurcation present a special interest, since for certain load paths one can find modes involving a large number of unit cells in both directions!

The stability phenomena associated with elliptical section fibers are even richer. For periodic fiber distributions, microscopic and macroscopic onset-of-failure curves are found for both compression ($\varphi = \pi$) and tension ($\varphi = 0$) along the major axis of the fiber's elliptical section. The instability in the neighborhood of ($\varphi = \pi$) is due to the rotation of the fibers along their axes, which alleviates strain concentration. In contrast the instability about ($\varphi = 0$) is due to the appearance of eigenmodes with lower symmetry than the initial one, i.e., eigenmodes with fundamental cells larger than the unit cell of the composite's stress-free configuration. This observation is consistent with the results of Lopez-Pamies and Ponte Castañeda (2006a) for composites with random distributions of aligned fibers, and helps explain why a loss of ellipticity branch going through $\varphi = \pi$ can still be found, albeit at higher strains than the periodic square case with the same fiber volume fraction, while no such branch exists though $\varphi = 0$. Moreover in a rather large neighborhood of $\varphi = \pi$, and for the elliptical sections considered, the loss of ellipticity for both the periodic as well as the random microgeometry occurs prior to matrix cavitation. At this point one should also mention a rather surprising result for the stability of an imperfect composite, obtained from its perfect square microgeometry counterpart by a small perturbation of the fiber centers but not of their orientation. It is found that for loading paths with compression along the fiber section's major axis, near $\varphi = \pi$ but with $\varphi \neq \pi$, the imperfect aggregate loses its stability prior to its perfect counterpart, while the reverse situation exists for loading paths with tension along the fiber section's major axis, for the entire branch going through $\varphi = 0$. In this connection, we should also mention the recent numerical simulations of Moraleda et al. (2009) for composites with

random distributions of perfectly aligned fibers. While these simulations also gave fairly good agreement with the theoretical estimates of Lopez-Pamies and Ponte Castañeda (2006b), these authors did not observe loss of ellipticity for these materials, in contrast with the results of the present work for periodic and perturbed distributions of aligned fibers. Last but not least in the long list of interesting new phenomena, for the fiber sections with the highest aspect ratio ($r \geq 3$) the loss of macroscopic ellipticity curves have singularities in the neighborhood of $\varphi = \pi$, due to the dramatic change of the corresponding principal solution for even a small amount of shear.

In addition to the onset of macroscopic and microscopic instabilities, constraints to the principal solution due to fiber/matrix interface decohesion, matrix cavitation and fiber contact have also been addressed, thus giving a complete picture of the sequence at which the different failure mechanisms occur in this class of elastomeric composites. In fact, these instabilities are expected to dominate for the fiber-reinforced elastomers, except for loadings involving significant compression of the fibers, when such fibers have sufficiently large aspect ratio and stiffness leading to the development of macroscopic instabilities at relatively small macroscopic strains.

We have investigated here the rich stability behavior of a rather large class of fiber-reinforced elastomeric composites. However we feel that this is only the beginning, since many more questions have risen from this investigation. For example, the very intriguing relation between the stability of the perfect and corresponding imperfect microgeometry composites requires the calculation of post-bifurcated solutions for a proper explanation, in the spirit of Koiter's imperfection sensitivity theory. Although the exact nature of the matrix constitutive law is not important for elastomers, as our comparison between neo-Hookean and Gent matrix calculations has shown, this need not be the case for non-elastomeric materials. And of course there is the issue of stability of these composites under a full three-dimensional loading, which adds to the list of future investigation directions based on the present work.

Acknowledgments

The authors gratefully acknowledge support from SUNY at Stony Brook (O.L.-P.), NSF Grant DMS-0708271 (P.P.C.) and the Ecole Polytechnique (N.T.).

Appendix A. Constraints on the onset-of-failure curves

As mentioned in Section 4, there are criteria other than the loss of uniqueness or of rank-one convexity that can signal failure of the fiber-reinforced elastomer. These are (a) decohesion at the fiber/matrix interface, (b) cavitation at the matrix due to the presence of large hydrostatic tension and (c) fiber contact.

A.1. Fiber/matrix interface decohesion

Fiber/matrix decohesion is modeled here via a stress-based criterion. More specifically, whenever along any arbitrary loading path

$$\min_{\mathbf{x}\in\Gamma}\{\delta_c\mu_m - n_i(\mathbf{x})\sigma_{ij}(\mathbf{x})n_j(\mathbf{x})\} = 0, \tag{A.1}$$

decohesion ensues. In the above expression, $\mathbf{n}$ is the unit vector normal to the fiber/matrix interface Γ in the deformed configuration, $\boldsymbol{\sigma}$ is the Cauchy stress, each evaluated at a point $\mathbf{x}$ on the boundary of the fiber's cross-section, δ_c is a scalar indicating the strength of the interface and μ_m is the shear modulus of the matrix phase in the ground state.

Since all calculations are done in a Lagrangian setting, the field quantities in (A.1) must be expressed in terms of their reference configuration counterparts. The Cauchy stress tensor $\boldsymbol{\sigma}$ is related to the first nominal stress tensor $\mathbf{S}$ via the relation:

$$\sigma_{ij} = \frac{1}{\det\mathbf{F}} S_{ik}F_{jk}. \tag{A.2}$$

Furthermore, from Nanson's relation, the unit normal vector $\mathbf{n}$ in the deformed configuration and the element area da are related to their reference configuration counterparts $\mathbf{N}$ and dA via

$$n_j\, da = \det\mathbf{F} N_i F^{-1}_{ij}\, dA. \tag{A.3}$$

Making use of (A.2) and (A.3), the condition (A.1) can then be rewritten in the undeformed configuration.

Within the context of the S.O.H. estimates utilized in this work, the deformation — and therefore the stress — is uniform in the fibers. This allows to simplify considerably the evaluation of criterion (A.1), since the decohesion criterion can be rewritten entirely in terms of the constant deformation gradient field $\overline{\mathbf{F}}^{(2)}$ inside the fibers given by expression (3.6).

For the F.E.M. calculations the criterion (A.1) is evaluated numerically, over all interface elements, in the reference configuration with the help of (A.2) and (A.3).

A.2. Matrix cavitation

It is well known (see, e.g., Gent and Lindley, 1959) that under loading conditions with a sufficiently large hydrostatic stress component, elastomers may exhibit cavitation. In order to account for this phenomenon, we presently make use of an approximate criterion recently proposed by Lopez-Pamies (2009) for the onset of cavitation in compressible isotropic hyperelastic solids under general plane-strain loading conditions. The criterion states that for a hyperelastic material with stored-energy function $W(I,J)$, cavitation will occur at a material point whenever along a given loading path the deformation at that point first satisfies the condition:

$$2\frac{\partial W}{\partial I}(I,J)-\frac{\partial W}{\partial J}(I,J)=0. \tag{A.4}$$

The general criterion (A.4) applied to the neo-Hokean matrix chosen here (4.2) specializes to

$$1+J-\left(\frac{\kappa}{\mu}-1\right)J(J-1)=0. \tag{A.5}$$

Note that this condition depends only on the dilatational part of the deformation, as measured by J, and not on the distortional part I. In addition, relation (A.5) is seen to depend on the parameters μ and κ only through the ratio κ/μ, which measures the compressibility of the matrix.

The S.O.H. does not provide estimates for the pointwise deformation and stress fields and therefore cannot be utilized to inquire for the onset of cavitation in the matrix. Matrix cavitation can only be calculated by the F.E.M. which gives deformation fields at all the integration points in each element. The cavitation results presented here are based on the average deformation gradient of each element, since this method gives results that are not very sensitive to the chosen mesh.

A.3. Fiber contact

The loading of the elastomeric composites considered here may result into adjacent fibers coming into contact, leading to a percolating network of stiff fibers. Finding the strain combination in macroscopic strain space that leads to fiber contact is straightforward in the case of periodic composites but intractable for the random ones.

Fiber contact results are only given for the F.E.M. calculations in periodic elastomers. Exact expressions can be derived (assuming perfectly rigid fibers) for arbitrary loading in the case of circular section fibers ($r=1$). For the square microgeometry case, contact occurs when

$$\min_{\varepsilon_1,\gamma}\{\exp(2\varepsilon_1),\ \gamma^2+\exp(-2\varepsilon_1),(\gamma-\exp(\varepsilon_1))^2+\exp(-2\varepsilon_1)\}=\frac{4f_0}{\pi}. \tag{A.6}$$

For the hexagonal case, contact occurs when

$$\min_{\varepsilon_1,\gamma}\left\{\exp(2\varepsilon_1),\frac{3}{\exp(2\varepsilon_1)},\frac{3}{4}\left[\left(\gamma-\frac{\exp(\varepsilon_1)}{\sqrt{3}}\right)^2+\exp(-2\varepsilon_1)\right],\frac{1}{4}\left[\left(\gamma-\frac{\sqrt{3}}{\exp(\varepsilon_1)}\right)^2+\exp(2\varepsilon_1)\right]\right\}=\frac{2\sqrt{3}f_0}{\pi}. \tag{A.7}$$

For isochoric loading with $\gamma\neq 0$ and elliptical fibers ($r>1$), an approximate numerical calculation is needed, due to unknown fiber rotation which depends on the unit cell's equilibrium solution. The approximate contact criterion adopted is that contact occurs when the smallest distance between adjacent fibers d_{min} falls below a critical length, i.e., $d_{min}\leq 0.005L_1$, where L_1 is the X_1 dimension of the unit cell in the reference configuration. The choice of the tolerance parameter 0.005 is dictated by the requirement of a less than 1% error in the contact conditions for the no rotation case $\gamma=0$, where this condition can be calculated exactly from geometry (assuming again perfectly rigid fibers).

Appendix B. Expressions for the microstructural tensor P

In this appendix, we provide explicit expressions for the (in-plane) components of the tensor **P**, which serve to characterize the three types of microstructures (in the reference configuration) considered in this work: (i) periodic square, (ii) periodic hexagonal, and (iii) random isotropic distribution of aligned fibers with initially elliptical cross-section.

B.1. Periodic rectangular distribution

The microstructural tensor **P** for a rectangular distribution of fibers with elliptical cross-section may be written as (see, e.g., Suquet, 1990a,b)

$$P_{ijkl}=\frac{1}{\pi(1-f_0)}\sum_{\substack{p=-\infty\\ -\{p=q=0\}}}^{+\infty}\sum_{q=-\infty}^{+\infty}(L_{imkn}\xi_m\xi_n)^{-1}\xi_j\xi_l\frac{J_1^2\left(2\sqrt{\pi f_0}\sqrt{\frac{1}{\nu}p^2+\nu q^2}\right)}{\frac{1}{\nu}p^2+\nu q^2}, \tag{B.1}$$

where $\xi_1 = p$, $\xi_2 = \omega_c q$, and $\nu = \omega_c/\omega_f$. In these expressions, $J_1(\cdot)$ stands for the Bessel function of first kind, while ω_c and ω_f denote, respectively, the aspect ratio of the rectangular unit cell and the aspect ratio of the fibers — that is, $\omega_c = L_1/L_2$ and $\omega_f = r$ in Fig. 1b. Thus, for the square distribution $\omega_c = 1$, whereas for the hexagonal distribution $\omega_c = 2/\sqrt{3}$.

B.2. Random isotropic distribution

The microstructural tensor **P** for the random isotropic distribution of aligned fibers with elliptical cross-section may be expressed as (see, e.g., Ponte Castañeda and Willis (1995))

$$P_{ijkl} = \frac{r}{2\pi(1-f_0)}\int_0^{2\pi} \frac{(L_{imkn}\xi_m\xi_n)^{-1}\xi_j\xi_l}{r^2\xi_1^2+\xi_2^2}\,\mathrm{d}\theta - \frac{f_0}{2\pi(1-f_0)}\int_0^{2\pi}(L_{imkn}\xi_m\xi_n)^{-1}\xi_j\xi_l\,\mathrm{d}\theta, \tag{B.2}$$

where $\xi_1 = \cos\theta$ and $\xi_2 = \sin\theta$.

References

Abeyaratne, R., Triantafyllidis, N., 1984. An investigation of localization in a porous elastic material using homogenization theory. J. Appl. Mech. 51, 481–486.

Ball, J.M., 1977. Convexity conditions and existence theorems in nonlinear elasticity. Arch. Ration. Mech. Anal. 63, 337–403.

Bertoldi, K., Boyce, M., Deschanel, S., Prange, S.M., Mullin, T., 2008. Mechanics of deformation-triggered pattern transformations and superelastic behavior in periodic elastomeric structures. J. Mech. Phys. Solids 56, 2642–2668.

Braides, A., 1985. Homogenization of some almost periodic coercive functionals. Rend. Accad. Naz. XL 9, 313–322.

Brun, M., Lopez-Pamies, O., Ponte Castañeda, P., 2007. Homogenization estimates for fiber-reinforced elastomers with periodic microstructures. Int. J. Solids Struct. 44, 5953–5979.

Gent, A.N., Lindley, P.B., 1959. Internal rupture of bonded rubber cylinders in tension. Proc. R. Soc. A 249, 195–205.

Geymonat, G., Müller, S., Triantafyllidis, N., 1993. Homogenization of nonlinearly elastic materials, microscopic bifurcation and macroscopic loss of rank-one convexity. Arch. Ration. Mech. Anal. 122, 231–290.

Gong, L., Kyriakides, S., Triantafyllidis, N., 2005. On the stability of Kelvin cell foams under compressive loads. J. Mech. Phys. Solids 53, 771–794.

Hill, R., 1972. On constitutive macro-variables for heterogeneous solids at finite strain. Proc. R. Soc. A 326, 131–147.

Lahellec, N., Mazerolle, F., Michel, J.C., 2004. Second-order estimate of the macroscopic behavior of periodic hyperelastic composites: theory and experimental validation. J. Mech. Phys. Solids 52, 27–49.

Lopez-Pamies, O., Ponte Castañeda, P., 2006a. On the overall behavior, microstructure evolution, and macroscopic stability in reinforced rubbers at large deformations: I—theory. J. Mech. Phys. Solids 54, 807–830.

Lopez-Pamies, O., Ponte Castañeda, P., 2006b. On the overall behavior, microstructure evolution, and macroscopic stability in reinforced rubbers at large deformations: II—application to cylindrical fibers. J. Mech. Phys. Solids 54, 831–863.

Lopez-Pamies, O., 2009. Onset of cavitation in compressible, isotropic, hyperelastic solids. J. Elasticity 94, 115–145.

Malvern, L.E., 1969. Introduction to the Mechanics of a Continuous Medium. Prentice-Hall, Englewood Cliffs, NJ.

Marcellini, P., 1978. Periodic solutions and homogenization of nonlinear variational problems. Ann. Mat. Pura Appl. 4, 139–152.

Michel, J.-C., Lopez-Pamies, O., Ponte Castañeda, P., Triantafyllidis, N., 2007. Microscopic and macroscopic instability in finitely strained solids. J. Mech. Phys. Solids 55, 900–938.

Michel, J.-C., Ponte Castañeda, P., 2009. Unpublished work.

Moraleda, J., Segurado, J., Llorca, J., 2009. Finite deformation of incompressible fiber-reinforced elastomers: a computational micromechanics approach. J. Mech. Phys. Solids 57, 1596–1613.

Müller, S., 1987. Homogenization of nonconvex integral functionals and cellular elastic materials. Arch. Ration. Mech. Anal. 99, 189–212.

Nemat-Nasser, S., Iwakuma, T., Hejazi, M., 1982. On composites with periodic structure. Mech. Mater. 1, 239–267.

Nestorović, M., Triantafyllidis, N., 2004. Onset of failure in finitely strained layered composites subjected to combined normal and shear loading. J. Mech. Phys. Solids 52, 941–974.

Ponte Castañeda, P., 1989. The overall constitutive behaviour of nonlinear elastic composites. Proc. R. Soc. A 422, 147–171.

Ponte Castañeda, P., 1996. Exact second order estimates for the effective mechanical properties of nonlinear composite materials. J. Mech. Phys. Solids 44, 827–862.

Ponte Castañeda, P., Tiberio, E., 2000. A second-order homogenization method in finite elasticity and applications to black-filled elastomers. J. Mech. Phys. Solids 48, 1389–1411.

Ponte Castañeda, P., 2002. Second-order homogenization estimates for nonlinear composites incorporating field fluctuations I. Theory. J. Mech. Phys. Solids 50, 737–757.

Ponte Castañeda, P., Willis, J.R., 1995. The effect of spatial distribution on the effective behavior of composite materials and cracked media. J. Mech. Phys. Solids 43, 1919–1951.

Suquet, P., 1990a. Une méthode simplifiée pour le calcul des propriétés élastiques de matériaux hétérogènes à structure périodique. C. R. Acad. Sci. Paris 311, 769–774.

Suquet, P., 1990b. Méthodes de calcul simplifiées pour la détermination des propriétés élastiques linéaires de composites à structure périodique, Internal Report, L.M.A. Marseille.

Triantafyllidis, N., Maker, B.N., 1985. On the comparison between microscopic and macroscopic instability mechanisms in a class of fiber-reinforced composites. J. Appl. Mech. 52, 794–800.

Triantafyllidis, N., Bardenhagen, S.G., 1996. The influence of scale size on the stability of periodic solids and the role of associated higher order gradient continuum models. J. Mech. Phys. Solids 44, 1891–1928.

Triantafyllidis, N., Schraad, M.W., 1998. Onset of failure in aluminum honeycombs under general in-plane loading. J. Mech. Phys. Solids 46, 1089–1124.

Triantafyllidis, N., Nestorović, M.D., Schraad, M.W., 2006. Failure surfaces for finitely strained two-phase periodic solids under general in-plane loading. J. Appl. Mech. 73, 505–515.

Willis, J.R., 1977. Bounds and self-consistent estimates for the overall moduli of anisotropic composites. J. Mech. Phys. Solids 25, 185–202.